PONTIFICIA UNIVERSIDAD CATOLICA DE CHILE
ESCUELA DE INGENIERIA

TECTONIC ROLE OF MARGIN-PARALLEL AND MARGIN-TRANSVERSE FAULTS DURING OBLIQUE SUBDUCTION AT THE SOUTHERN VOLCANIC ZONE OF THE ANDES

ASHLEY STANTON-YONGE SESNIC

Thesis submitted to the Office of Research and Graduate Studies in partial fulfillment of the requirements for the Degree of Master of Science in Engineering

Advisors:
JOSÉ CEMBRANO
W. ASHLEY GRIFFITH

Santiago de Chile, (July, 2016)

PONTIFICIA UNIVERSIDAD CATOLICA DE CHILE
ESCUELA DE INGENIERIA

TECTONIC ROLE OF MARGIN-PARALLEL AND MARGIN-TRANSVERSE FAULTS DURING OBLIQUE SUBDUCTION AT THE SOUTHERN VOLCANIC ZONE OF THE ANDES

ASHLEY STANTON-YONGE SESNIC

Members of the Committee:

JOSÉ CEMBRANO

W. ASHLEY GRIFFITH

DANIEL HURTADO

CONSTANTINO MPODOZIS

ÁLVARO SOTO

Thesis submitted to the Office of Research and Graduate Studies in partial fulfillment of the requirements for the Degree of Master of Science in Engineering

Santiago de Chile, (July, 2016)

El goce está en el recorrido y no en el destino

En el aprendizaje y no en el conocimiento

En el proceso y no en el término.

ACKNOWLEDGEMENTS

I would like to thank my professor José Cembrano for the countless field days, conversations and coffees, when the lessons of science and life took place. Thank you for guiding me into the geo-science path. For his hospitality, patience and guidance I would like to thank my co-advisor W. Ashley Griffith. I am very grateful to professor Constantino Mpodozis for his fruitful comments and suggestions that helped to considerably improve this thesis. Thank you to my geo-friends Tomás, Pablo, Rodrigo, Pamela, Álvaro, Nico, Naty, Tiaren and Felipe for making this process full of warmth and friendship and to my geo-professors Gonzalo and Gloria for their closeness and support. I am very grateful to Mariel for always thinking in the little details, which are not so little after all. To my office-mates from La Pecera, thank you for the every-day conversations, laughs and cuchuflís. Thank you to Rene for facilitating everything for me during my stay in the United States, you were a great host.

This research was financially supported by FONDECYT project n°1141139 and FONDAP Project 15090013 'Centro de Excelencia en Geotermia de los Andes'. I am also very grateful for the support by CONICYT's national Master's scholarship.

Thanks to my family: mum, dad, Baba, Nicole and Cata for their unconditional love and support without which I could not have become who I am and could have never completed this thesis. Finally, thanks to Gerd for being always there for me and for helping me in every possible way.

GENERAL INDEX

Page

TABLES INDEX

Page

FIGURES INDEX

Page

RESUMEN

Los márgenes tectónicos caracterizados por subducción oblicua tienden a desarrollar sistemas de falla paralelos al margen en la placa cabalgante, los cuales son responsables del crecimiento de cadenas montañosas y de la partición de la deformación interplaca. Sin embargo, en estos ambientes tectónicos también es común encontrar fallas transversales al orógeno, las que han sido ampliamente ignoradas en los análisis de partición de deformación. Es relevante entonces establecer si los sistemas de falla transversales cumplen un rol en la acomodación de deformación tectónica resultante de la subducción oblicua. Mediante la implementación de un modelo 3D de la subducción en el margen andino de Chile utilizando el método de los Elementos de Borde, fue posible determinar la respuesta elástica de fallas de distinta orientación durante las etapas del ciclo sísmico de subducción (CSS). Los resultados muestran que el sistema de falla de Liquiñe Ofqui (SFLO), paralelo al margen, exhibe una cinemática de largo plazo dextral-inversa durante el período intersísmico del CSS con un deslizamiento oblicuo a tasas de 1 a 7 mm/año. Fallas de rumbo NW deslizan con una cinemática sinistral-inversa a una tasa de 1.4 mm/año mientras que fallas de rumbo ENE exhiben una cinemática de rumbo dextral a 0.85 mm/año. Durante el período cosísmico del CSS todas las fallas modeladas invierten sus cinemáticas: fallas ENE adquieren una cinemática sinistral y fallas NW exhiben un deslizamiento normal-dextral. Esta tensión cosísmica en fallas NW puede ser significativa (hasta 0.6 MPa) lo cual sugiere que estas fallas pueden comportarse como canales transientes de transporte de magma a través de la corteza. Los resultados del modelo demuestran que la partición de la deformación es un proceso más complejo de lo reconocido hasta la fecha: fallas transversales son capaces de absorber significativa deformación resultante de la convergencia oblicua, comúnmente atribuida sólo a fallas paralelas al margen. El deslizamiento en fallas transversales puede desencadenar terremotos corticales con una magnitud máxima de Mw 6.0 a 6.7 mientras en trazas del SFLO pueden esperarse terremotos de un rango de Mw 6.2 a 6.9.

ABSTRACT

Obliquely convergent subduction margins develop trench-parallel faults shaping the regional architecture of orogenic belts and partitioning interplate deformation. However, transverse faults also are common along most orogenic belts, although have been largely neglected in strain partitioning analysis. It is then relevant to assess whether and how transverse faults accommodate plate-margin deformation arising from oblique subduction. Here, the kinematics and slip rates of differently oriented faults are constrained to assess their tectonic role in strain partitioning. Through the implementation a forward 3D boundary element model (BEM) of subduction at the Chilean margin, the elastic response of intra-arc faults during different stages of the Andean subduction seismic cycle (SSC) is evaluated. The model results show that the margin-parallel, NNE-striking Liquiñe-Ofqui Fault System (LOFS) accommodates dextral-reverse slip during the interseismic period of the SSC, with oblique slip rates ranging between 1-7 mm/yr. NW-striking faults exhibit sinistral-reverse kinematics during the interseismic phase of the SSC, accommodating a maximum oblique slip of 1.4 mm/yr. ENE-striking faults are dextral strike-slip with a maximum net slip of 0.85 mm/yr. During the SSC coseismic phase, all modeled faults switch their slip sense: NE-striking faults become sinistral whereas NW-striking faults are normal-dextral. Because coseismic tensile stress on NW faults can be significant (0.6 MPa) it is very likely that these faults can serve as transient magma pathways. The model demonstrates that slip partitioning is more complex than previously recognized: transverse faults are capable of absorbing a significant amount of plate-boundary deformation arising from oblique convergence, commonly attributed only to margin-parallel faults. The upper-bound magnitude for crustal earthquakes due to slip at NW and NE striking faults is on the range of Mw 6.0 to 6.7, whereas earthquakes ranging from Mw 6.2 to 6.9 can be expected at the LOFS.

1. INTRODUCTION

Understanding the nature of crustal deformation within convergent margins is crucial to unravel the processes responsible for orogenesis, crustal faulting and their link to subduction-related processes such as volcanism, as well as the consequent geologic hazards associated with these processes. This work intends to unravel how plate-boundary deformation within obliquely subduction margins is partitioned and accommodated at differently oriented crustal faults in an attempt to challenge the existent paradigm where strain partitioning and orogen-building due to oblique subduction is accommodated only at margin-parallel crustal faults. This regional-scale tectonic problem is addressed through a numerical modeling approach using the Boundary Element Method (BEM).

The first chapter of this manuscript consists of a brief description of the conceptual framework in which this research is contextualized, as well as the statement of the scientific problem that motivates this study, its hypothesis, specific objectives and theoretical background of the methodology used to address it. The development and outcome of this research, including model implementation, results, discussion and main conclusions, are described in chapter two of this manuscript consistent of the article *Tectonic role of margin-parallel and margin-transverse faults during oblique subduction in the Southern Volcanic Zone of the Andes: Insights from Boundary Element Modeling*, submitted to journal *Tectonics*.

1.1 Conceptual framework

1.1.1 Geological faults

A geological fault is a discontinuity between two masses of rock along which relative displacement has occurred. Faults exist within the earth's crust from the microscale (μm) to the continental scale (thousands of kilometers) and are responsible for the accommodation of a great part of deformation arising from interaction between tectonic plates. To facilitate the geometric description of a fault, it is often idealized as a plane whose orientation is defined by two angles: its strike ρ and dip μ (Figure 1-1). The strike of a fault plane is the angle between the north and the strike vector, which is the intersection of the fault plane with the horizontal plane; the dip represents the angle of maximum slope of the fault plane, measured in a vertical plane perpendicular to the strike vector (Figure 1-1a).

Faults can be classified according to whether the relative movement between the blocks defined by the fault plane occurs up and down the fault (dip-slip faults) or along the fault plane (strike-slip faults). In dip-slip faults, if the movement is up-dip the fault is called reverse or thrust (Figure 1-1c) whereas if it is down-dip the fault is normal (Figure 1-1b). Strike-slip faults can be dextral (also called right-lateral) or sinistral (left-lateral) (Figure 1-1d,e). Oblique-slip faults are those which display a component of dip-slip and strike-slip simultaneously (Figure 1-1f).

Anderson's theory of faulting [*Anderson*, 1951] simplifies the mechanics of faulting by assuming that two of the three principal axis of stress are parallel to the surface of the earth, and thus the third one is vertical. In this context, thrust faults form when σ_1 (the most compressive stress) is horizontal and σ_3 is vertical (Figure 1-1c) whereas normal faults occur with vertical σ_1 and horizontal σ_3 (Figure 1-1b). Strike-slip faults form with horizontal σ_1, σ_3 and verticalσ_2 (Figure 1-1d, e).

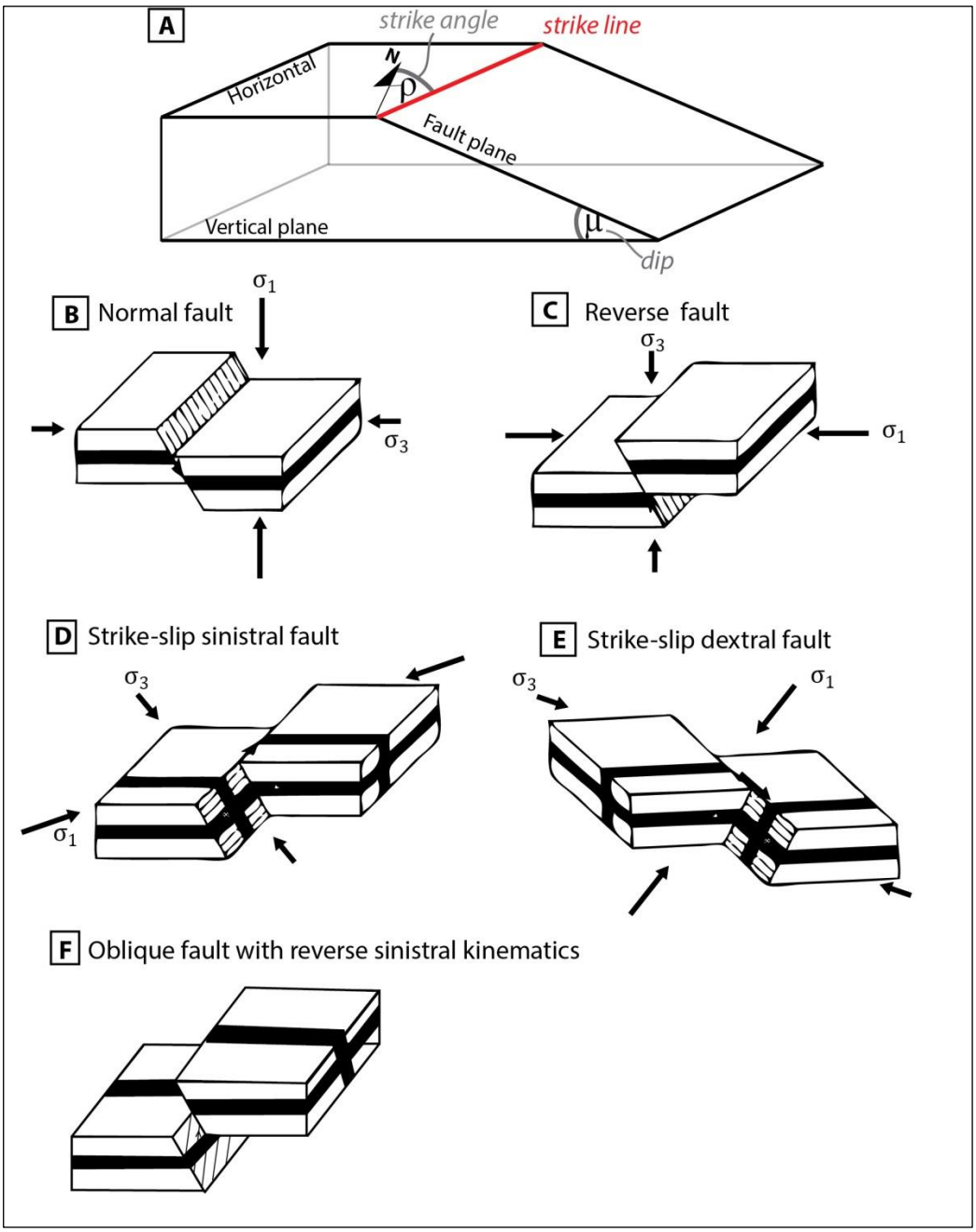

Figure2-1. A) Geometrical description of a fault plane in terms of strike ρ (strike line is shown in red) and dip μ. B) Dip-slip fault with normal kinematics. C) Dip-slip fault with reverse kinematics. D) Strike-slip fault with sinistral kinematics, E) Strike-slip fault with dextral kinematics and F) Oblique fault with reverse sinistral kinematics. Orientation of the principal axis of stress according to Anderson's theory of faulting is shown for each fault kinematics. Modified after earthsci.org web figure.

An earthquake takes place when a rupture dynamically propagates through the crust across a fault surface. The stored elastic energy is released through several mechanisms, including seismic wave radiation that propagate though the surrounding rock until they reach the surface, heat flow and work against gravity [e.g. *Scholz,* 2002; *Newman and Griffith*, 2014]. Seismic instrumentation across the Earth's crust allows detection of first-motions or polarity of body waves resulting from an earthquake, which can be compressional or dilatational depending on the geometry of the fault plane, its kinematics and the relative position of the seismic instrument with respect to the fault. The direction and nature of first-motion P-waves registered by several seismometers can be plotted in a lower-hemisphere equal-area projection, determining the spatial distribution of tensile and compressional stress resulting from an earthquake. The result is the focal mechanism of the earthquake, which indicates two possible orientations for the plane of rupture (the fault plane and anodal plane) and its kinematics in terms of the direction of the tension axis (T or σ_3) and the direction of the maximum compressive axis (P or σ_1) [*Sipkin*, 1994]. Examples of focal mechanisms for strike-slip, normal, reverse and oblique faults are shown in Figure 1-2.

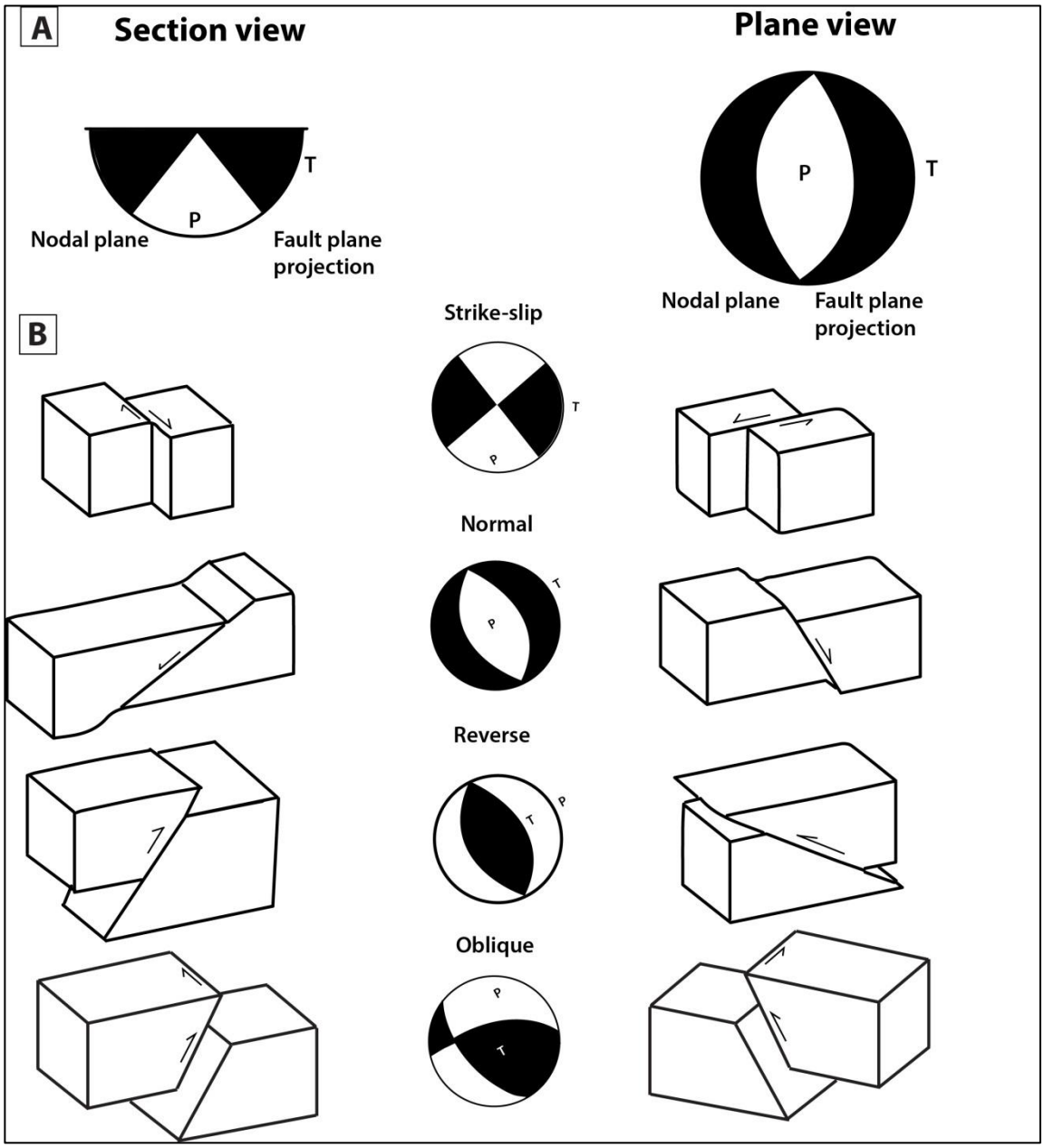

Figure 1-2. Schematic diagram of earthquake focal mechanisms. A) Section view of a fault plane with normal kinematics and its nodal/auxiliary plane cross-cutting a lower-hemisphere sphere. Stress distribution because of the fault is represented by black dihedra for tension and white dihedra for compression. The plane view represents the intersection of the planes with the sphere, which delimit the tension and compression dihedra. B) Strike-slip, normal and reverse focal mechanisms with corresponding block diagrams showing kinematics of both of the possible fault planes. Oblique-slip transpressional focal mechanism is shown as an example of a combination of sip-slip and strike-slip motions. Modified after USGS web figure.

1.1.2 Subduction plate-boundaries

Convergent plate-boundaries are those where the relative movement between two tectonic plates causes them to collide; subduction plate-boundaries occur when one of the convergent plates descends beneath the other. Subduction margins concentrate the majority of the largest earthquakes recorded on Earth, which occur due to slip at the major fault plane defined by the plate interface. The time-lapse between megathrust earthquakes at a subduction margin is known as the interseismic phase of the subduction seismic cycle (SSC), which can extend over hundreds of years for large events. During this period, shear stress due to tectonic motion builds up on an area of the plate interface where coupling between the overriding and underlying plates does not allow slip. This area is known as the locked zone and/or seismogenic zone. When the failure stress is reached, an earthquake is nucleated and propagated along the plate interface releasing the stored energy and causing an elastic rebound at the overriding plate (Figure 1-3c). This quasi-instantaneous process constitutes the coseismic phase of the SSC which, according to geodetic analysis, is limited to the seconds to minutes constituting the duration of the mainshock [*e.g. Vigny et al.*, 2011; *Moreno et al.*, 2012]. Aseismic afterslip commonly follows a megathrust earthquake, consisting of discrete pulses of creep events which decay in frequency following the mainshock [*Marone et al.*, 1991]. Additionally, deformation at the upper crust may continue months to years after a megathrust earthquake as a result of viscous relaxation of the underlying mantle [*e.g. Hu et al.*, 2004]. These two processes (afterslip and viscous mantle relaxation) constitute the post-seismic phase of the subduction seismic cycle.

According to the above stated definition of the stages of the SSC, the crust behaves as an elastic material that releases the accumulated interseismic deformation through megathrust earthquakes and post-seismic deformation. However, if this were completely accurate, no permanent deformation should be recorded at the overriding plate and thus no mountain building would take place within subduction margins. Studies of orogen-

building thrust faults show that over geologic time (*i.e.*, millions of years) around 10% of plate convergence is accommodated by upper-plate permanent deformation and orogenesis; the rest is released by elastic rebound during the SSC [*e.g.*, *Jordan et al.*, 1993]. Nonetheless, simple elastic models of strain accumulation and release provide useful first-order understanding of the deformation cycle at subduction zones [*Savage*, 1983; *Bevis and Martel*, 2001].

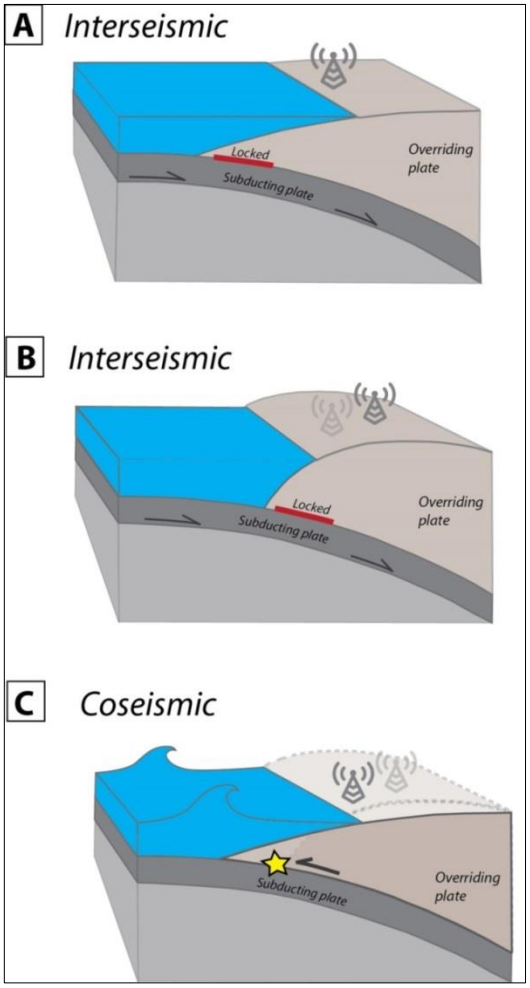

Figure 1-3. Subduction seismic cycle. A) Interseismic phase: the subducting plate descends beneath the overriding plate while a portion of the plate's interface remains locked. B) Stress builds up in the locked portion of the plate's interface while the overriding plate experiences compression and inland displacement, illustrated by the displacement of a GPS antenna. C) Coseismic phase: an earthquake nucleates on the plate interface releasing the locked zone. The overriding plate experiences a quasi-instantaneous extension as a result of the elastic rebound and up-dip slip. Subsidence on the oceanic floor may induce a tsunami.

Volcanism is closely related to subduction plate boundaries. A belt of regularly spaced volcanoes, usually parallel to the trench, commonly lies at the overriding plate of a subduction margin at a distance of ca. 200 km from the trench. The subducting oceanic crust is dehydrated while dragged down towards the mantle, favoring hydrous melting of the slab at the mantle wedge [*Peacock*, 1991]. Partially-melted mantle rocks are sufficiently buoyant to generate an ascending flow and enhance melting through pressure release [*Turcotte and Schubert*, 2014]. A source of ascending magma is thus generated at the mantle wedge, which episodically reaches the surface creating and feeding volcanic complexes. This belt of volcanoes above the mantle wedge is known as volcanic arc, which defines an area of thermally weakened lithosphere called the intra-arc region. The region in between the trench and the intra-arc is called fore-arc, whereas the region behind the volcanic arc is known as back-arc (Figure 1-4).

The direction and magnitude of relative convergence between plates at subduction margins in known as convergence vector, which commonly displays a certain degree of obliquity with respect to the trench-orthogonal vector. It has been observed that oblique convergence can be decomposed into a margin-orthogonal component and a margin-parallel component [*e.g. Fitch* 1972; *Jarrard* 1986; *Beck* 1991, 1993] (Figure 1-4). Evidence of this slip partitioning process has been found on obliquely subducting margins where the trench-parallel component of deformation is accommodated at margin-parallel strike-slip faults within the thermally weakened intra-arc region at the overriding plate, *e.g.* Sumatra [*Fitch,* 1972], Eastern Turkey [*Jackson, 1992*], New Zealand [*Cashman et al.*, 1992], Chile [*Beck* 1991]. The margin-orthogonal component arising from oblique convergence, in turn, is mostly accommodated through elastic rebound during the subduction seismic cycle and at margin-parallel thrust faults which shape the main architecture of orogenic belts.

Conclusive evidence of slip partitioning taking place at subduction margins can be obtained from the observation of slip vectors of thrust earthquakes, which are commonly

rotated away from the direction of plate convergence and toward the trench-normal [*Jarrard,* 1986a; *McCaffrey*, 1992, 1993; *Yu et al.*, 1993]. Two end-member scenarios of slip partitioning mechanism can then be established: 1) Complete slip partitioning where slip vectors of thrust earthquakes are parallel to the trench-orthogonal vector, meaning that slip at the plate's interface is completely dip-slip and all the margin-parallel component of deformation is accommodated at a strike-slip fault within the overriding plate and a fore-arc sliver translation is thus expected (Figure 1-5a) and 2) No slip partitioning at all where the upper plate acts as a coherent elastic unit and slip vectors of thrust earthquakes are parallel to the convergence vector (Figure 1-5b). Most active subduction zones lie at some part of the spectrum defined by these two end members.

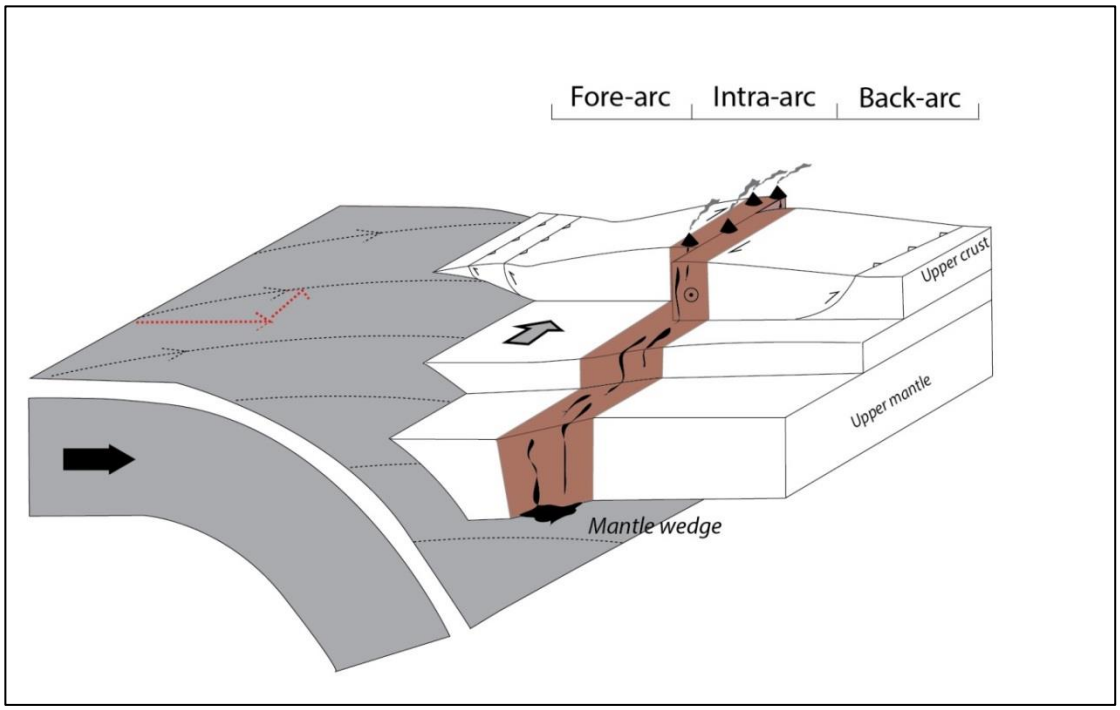

Figure 1-4. Schematic illustration showing the first-order architecture of oblique subduction. Convergence vector can be decoupled into a margin-orthogonal component and a margin-parallel component, shown in dashed red arrows, as a result of strain-partitioning. The margin-orthogonal component is accommodated at the plate's interface and at margin-parallel thrust faults at the fore-arc and back-arc regions. The margin-parallel component can be accommodated at margin-parallel strike-slip faults at the thermally weakened crust of the intra-arc. Modified after *De Saint Blanquat et al.*, 1998.

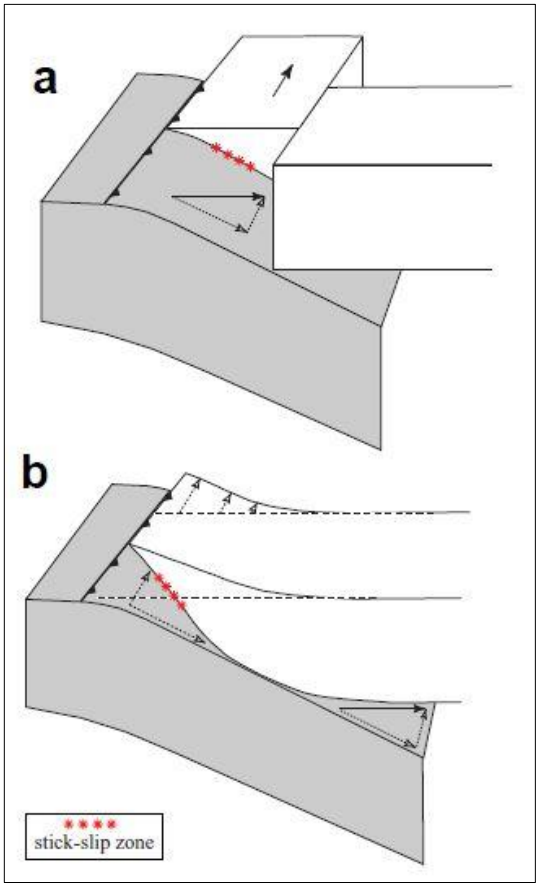

Figure 1-5. Schematic illustrations of the partitioning of oblique convergence at subduction zones. A) Complete partitioning by the development of a fore-arc sliver and B) Distributed deformation on a mechanically coherent fore-arc. [*Bevis and Martel,* 2001].

1.1.3 Tectonic control of magma transport through the lithosphere

Numerous studies of intra-arc geologic structures and analog models have concluded that faults are closely related to magma transport and emplacement in any type of tectonic setting [*Cembrano and Lara*, 2009]; either strike-slip [*e.g. Hutton,* 1982], extensional [*e.g. Hutton*, 1988], compressive [*e.g. Brown and Solar*, 1998] transpressive

(*i.e.* compression plus shear), [*e.g. De Saint Blanquat* et al., 1998] or transtensive (*i.e.* extension plus shear), [*e.g. Guineberteau* et al., 1987].

Nakamura (1977) proposed that the systematic alignment of minor eruptive centers within volcanic complexes at subduction margins respond to the regional tectonic stress. The elongation of major volcanic complexes and alignment of minor eruptive centers (Fig1-6a) are believed to represent an analog of hydro fracture resulting from magma overpressure, which are expected to be oriented perpendicular to the minimum principal stress axis (least compressive stress axis) and sub-parallel to the maximum horizontal stress. The elongation and morphology of flank cones (Fig 1-6b) are believed to reflect the geometry and sometimes kinematics of underlying faults acting as magma pathways [*Tibaldi*, 1995; *Corazzato and Tibaldi*, 2006].

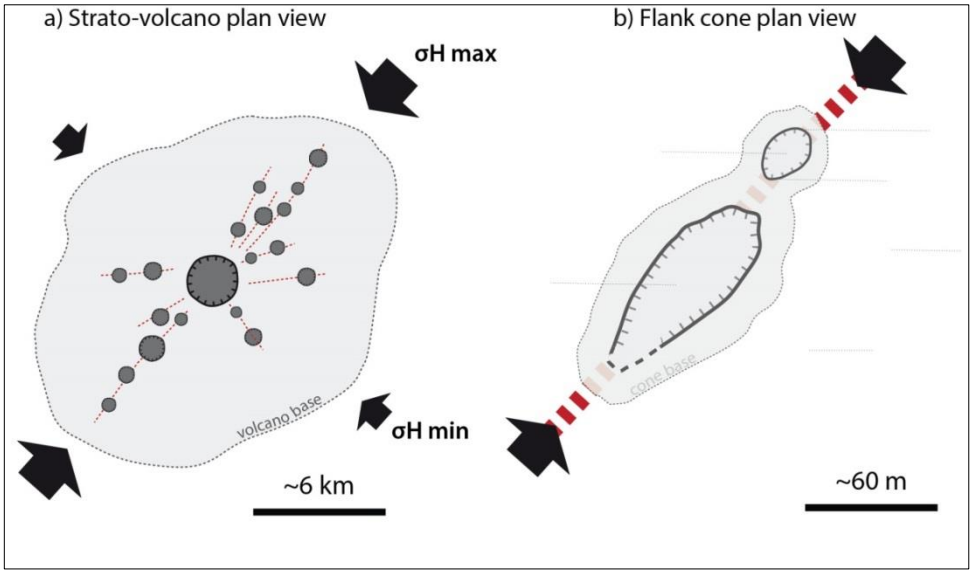

Figure 1-6. Traditional models for differential stress field dictating spatial distribution and geometry of elongated volcanoes and minor eruptive centers. A) *Nakamura* 1977 proposed that the volcano-scale orientation of $\sigma_{H\,Max}$ may be inferred from the alignment of minor eruptive centers and feeder dikes within strato-volcanoes. B) *Tibaldi,* 1995 and *Corazzato and Tibaldi,* 2006 models where the

elongation of flank cones indicate the geometry of the underlying magma-feeding fracture orientation (dashed red) [*Sielfeld et al.*, 2016].

Pre-existing faults are thought to play a fundamental control on the geometry and spatial distribution of minor eruptive centers and related feeder dikes [*Nakamura*, 1977; *Shaw*, 1980; *Brogi et al.*, 2010; *Sielfeld et al.*, 2016]. As a result, volcanic chains, elongated strato-volcanoes and flank cones alignments are thought to be the surface manifestation of underlying crustal faults. Because faults may have formed prior to magmatism, they may not be optimally oriented with respect to the current tectonic setting to activate and promote magma ascent. In these cases, fluid overpressure may reactivate the fault if it is oriented up to a critical angle with respect to σ_1, beyond that angle, tensile stress is required [*Sibson*, 1985].

1.2 Tectonic framework of the Andes

The Andes are a result of magmatic and tectonic activity operating along the western margin of South America since the late Neoproterozoic (800-700 Ma) [*Mpodozis and Cornejo*, 2012], even though the formal Andean tectonic cycle started at the Jurassic period (*ca*. 180 Ma) when subduction-related processes initiated and have operated continuously until the present-day. It is a region dominated by sedimentation, magmatism and tectonic deformation superimposed on a Paleozoic basement formed by accretion of terranes [*Mpodozis and Ramos*, 1989]. The Andean Cordillera currently constitutes the largest active orogenic system, developed along more than 8000 km from the Caribbean Sea to Tierra del Fuego [*Ramos*, 2009].

The current setting of the Andes at the Chilean margin until the Chile Triple Junction, Aysen (Figure 1-7), is characterized by the slightly oblique subduction of the oceanic Nazca plate underneath the South American plate at a rate of 66 mm/yr with a direction

of *ca*. N78°E [*Angermann et al.,* 1999; *Kendrick et al.,* 2003] (Figure 1-7). An active volcanic arc consistent of hundreds of active volcanoes and minor eruptive centers is present within distinguishable segments along the Andes. These segments are the Northern (5°N-2°S), Central (14°S-27°S), Southern (33°S-47°S) and Austral (49°S-55°S) Volcanic Zones [*Stern*, 2004]. Volcanic gaps in between these segments (*e.g.* Pampean flat-slab; Figure 1-7) occur where shallow subduction angles do not allow the development of a mantle wedge [*Jordan et al.,* 1983b; *Ramos et al.,* 2002].

South of 33°S the regional morphology of the Andes of Chile and Argentina is characterized by margin-parallel (close to North-South trending) morpho-tectonic units. From west to east, these units consist of: the Coastal Range, Central Depression, Principal Cordillera and Foreland region, where the active orogenic system consistent of major margin-parallel thrust faults and fold systems shape the well-organized N-S architecture of the Andean mountain belt (Figure 1-7).

Second-order transverse-to-the-orogen structures have also been recognized all along the Andes. [*e.g. Katz* 1971; *Yañez et al*., 1998; *Melnick and Echtler*, 2006; *Glodny et al.*, 2008], some of which are shown in Figure 1-7. For example, in the Andes of Northern Chile, NW-striking faults with predominantly left-lateral motion have been documented at the Altiplano-Puna Plateau (*e.g*. Calama-Olocapato-El Toro Fault Zone, Figure 1-7) [*Allmendinger et al.,* 1983; *Jordan et al.,* 1983]. Miocene-Quaternary volcanism has developed along these oblique-to-the-orogen faults, forming transverse volcanic chains [*Acocella et al.,* 2011; *Norini et al.,* 2013].

At Central Chile, *Yañez et al.,* (1998) described a major WNW-trending magnetic and gravimetric anomaly along the Maipo river valley: the Melipilla Anomaly (AM, Figure 1-7), spatially associated with the Melipilla Fault [*Wall et al*., 1996] which they associate with a major tectonic transition along the Andean margin. Furthermore, *Piquer et al.,* (2015) postulated that hydrothermal minerals related with the porphyry copper

deposits of central Chile (Rio Blanco, Los Bronces, El Teniente) precipitated along NW and NE-striking fault systems, although no conclusive evidence is presented to support this claim with respect to NW-striking faults.

Margin-oblique and seismically active faults have also occurred in the present-day fore-arc of Chile. Current tectonic activity has been shown for NW-striking fore-arc faults such as the Lanalhue Fault (LF, Figure 1-7) with sinistral kinematics [*Glodny et al.*,2008] and the Pichilemu Fault (PF, Figure 1-7) [*Aron et al.,* 2013, 2014] which hosted earthquakes of Mw 7.0 with normal kinematics eleven days after the Maule 2010 Mw 8.8 earthquake. In these works as well as in *Melnick et al.*, (2009), a clear association is postulated between these margin-transverse faults and seismic segmentation of the plate interface.

At the Southern Volcanic Zone of the Andes (SVZ) oblique-to-the-arc structures are abundant, represented by elongated major volcanic complexes and systematic alignments of flank volcanoes and minor eruptive centers oriented with NW and ENE strikes [*Melnick et al.*, 2006; *Sielfeld et al.*, 2016; *Pérez-Flores et al*, 2016; *Lara et al.*, 2004, 2006]. These volcanic alignments are believed to be the surface manifestation of basement faults exerting a fundamental control in quaternary volcanism [*Cembrano and Moreno*, 1994*; López-Escobar et al*., 1995; *Cembrano and Lara,* 2009].

Abundant evidence thus supports the existence of Andean Transverse Faults (ATF) and their relevance in controlling a variety of subduction related processes. However, whether and how these structures play a role in the accommodation of crustal deformation is not well understood. In this study, the question of the tectonic role of ATF is addressed in the intra-arc region of the SVZ, where poorly described ENE and NW-striking faults co-exist with margin-parallel fault systems within a complex tectonic setting, which is described in the following section.

1.2.1 Tectonic setting of the Southern Volcanic Zone of the Andes

The Southern Volcanic Zone of the Andes (SVZ) constitutes the volcanic arc between the latitudes of Santiago (33°S) and the Chile Triple Junction (CTJ) at the Taitao Peninsula (Aysen, 47°S) where the Nazca, South American and Antarctic plates meet. The Chile Rise (Figure 1-7), an actively spreading oceanic ridge, is currently colliding with the continental margin at the CTJ [*Forysthe and Nelson*, 1985]. The main fault domains at the SVZ are further described in the next sub-sections.

a) Margin-parallel structural domains: The Liquiñe-Ofqui Fault System

The main structural feature within the SVZ is the margin-parallel Liquiñe Ofqui Fault System (LOFS) [*Hervé*, 1994; *Cembrano et al.*, 1996], a major intra-arc, strike-slip fault system that runs for 1200 km from 38°S to 47°S (Figure 1-7). Long and short-term dextral slip along the LOFS is testified by exposed fault slip data [*Cembrano et al.*, 1996; *Pérez-Flores et al.*, 2016; *Vargas et al.*, 2013], mylonitic shear zones [*Cembrano et al.*, 2000], shallow focal mechanisms [*Chinn and Isacks*, 1983; *Lange et al.*, 2008; *Legrand et al.*, 2011] and paleomagnetic data showing a clock-wise rotation pattern east of the LOFS and counter-clock-wise rotation west of it [*Beck et al.*, 1993; *Rojas et al.*, 1994; *Hernández-Moreno et al.*, 2014, 2016].

The relatively steady right-oblique subduction of the Farallon (Nazca) plate beneath South America since 48 Ma [*Pardo-Casas and Molnar*, 1987] is believed to be a driven mechanism for the long-term dextral slip at the LOFS [*Beck et al.*, 1993; *Cembrano et al.*, 2000]. According to these authors, the margin-parallel component of oblique convergence is –at least- partially accommodated by dextral slip along the LOFS, which is facilitated by the weakening of the crust resulting from the thermal anomaly at the intra-arc. In these models, the block west of the fault (Chiloé Block) becomes a detached part of the continental crust (referred to as fore-arc sliver) with northward motion. Other

authors have emphasized the effect of the subduction of the Chile Rise at the southern termination of the LOFS in the northward displacement of the Chiloé Block [*Forysthe and Nelson*, 1985; *Thomson* 2002].

Field evidence on the LOFS has not been sufficient to properly constrain its depth geometry and approximated slip rate. A short-term slip rate for the Chiloé Block of 6.5 mm/yr was obtained by *Wang et al.,* (2007). A long-term slip along the LOFS was estimated using a kinematic model by *Rosenau et al.,* (2006), who obtained slip rates of 32 ± 6 mm/yr south of 40°S and 13 ± 3 mm/yr north from 40°S. However, this kinematic model is highly sensitive to parameters that are obtained without conclusive evidence.

Numerical modeling approaches using the Finite Element Method (FEM) have been implemented to study the stress field at the LOFS [*Islam*, 2009; *Iturrieta et al.*, 2015]. *Islam*, (2009) explored two possible origins for the stress field at the LOFS: oblique plate convergence and/or the collision of the Chile Rise. In this work, the author concludes that strike-slip displacement at the LOFS is likely to be driven by oblique collision of the Chile Rise at the CTJ. *Iturrieta et al.*, 2015 described the stress regime at the LOFS resulting from oblique subduction loadings, obtaining strike-slip to transpressive stress regimes at the main branches of the LOFS. These results suggest that oblique convergence alone can cause strike-slip displacement at the LOFS, which is favored by ridge collision to produce the observed kinematic behavior of the fault [*Cembrano et al.*, 2000].

b) Second-order transverse faults

Second-order structures at the SVZ are transverse-to-the-orogen faults, which are recognized as elongated strato-volcanoes, volcanic chains formed by two or more strato-

volcanoes and alignments of flank and monogenic cones [*López-Escobar et al.,* 1995; *Sielfeld et al.,* 2016; *Lara et al.,* 2004]. These intra-arc transverse faults are believed to be pre-Andean basement faults currently representing crustal weak zones allowing magma transport through the lithosphere and exerting a fundamental control on the spatial distribution and genesis of volcanic complexes, minor eruptive centers and geothermal springs [*e.g. Cembrano and Moreno,* 1994; *Melnick et al,* 2006; *Cembrano and Lara,* 2009; *Sánchez-Alfaro et al.,* 2013; *Pérez-Flores et al.,* 2016].

Two categories of this second-order transverse faults are recognized in the SVZ [*Cembrano and Lara,* 2009]: 1) ENE-striking faults which are sub-parallel to the regional direction of σ_1 [*Lavenu and Cembrano,* 1999; *Pérez-Flores et al.,* 2016] which, according to *Nakamura* (1977) and *Tibaldi* (1995) models, are oriented consistently to experience extension and promote magma and fluid ascent and 2) NW and WNW-striking faults which, according to the above stated models, have an inconsistent orientation with the regional tectonic regime to promote extension and thus favor magma ascent.

Field studies carried out on some of these intra-arc transverse faults testify that ENE-striking faults exhibit dextral-normal slip sense and favor the emplacement of ENE-striking dikes and veins [*Pérez-Flores et al.,* 2016; *Sielfeld et al.,* 2016]. NW-striking faults in turn, exhibit two kinematic behaviors: the first is characterized by sinistral-reverse slip sense, which is the compatible behavior with respect to the regional stress field. The second one shows normal faulting, which is with the regional stress field [*Roquer,* 2016; *Pérez-Flores et al.,* 2016]. Several studies have emphasized the role of the seismic cycle of subduction in the in the interplay between volcanism and tectonics in these NW-striking misoriented faults; the quasi-instantaneous stress regime produced due to the elastic rebound of the overriding plate during the coseismic phase of the SSC [*Aron et al.,* 2013, 2014] could trigger sudden extension in these faults, which in this scenario would be optimally oriented [*Lara et al.,* 2004, 2006; *Sepúlveda et al.,* 2005].

However, field evidence is limited to specific structural sites, restricting a wide understanding of these faults and not allowing estimating long and short-term slip rates and slip sense along them.

Figure 1-7. Tectonic setting of the Andes at Chile and Argentina. The active volcanic arc is clustered in segments (Central, Southern and Austral Volcanic Zones). Main structural domains are the margin-parallel thrust systems responsible for the active orogen-building and the also margin-parallel, strike-slip Liquiñe-Ofqui Fault System (LOFS) which accommodates dextral shear resulting from oblique convergence. Some Andean Transverse Faults are shown in dashed lines: the Calama-Olocapato-El Toro (COT) [*Acocella et al.*, 2011], Antofagasta-Calama Lineament (ACL) [*Arriagada et al.*, 2003], Melipilla Anomaly (MA) [*Yañez et al.*, 1998], Pichilemu Fault (PF) [*Aron et al.*, 2013], Lanalhue Fault (LF) [*Glodny et al*., 2008], Mocha-Villarrica Fault Zone (MVFZ) [*Melnick et al.*, 2006], among others. Kinematics is shown for ATF when supportive evidence is available.

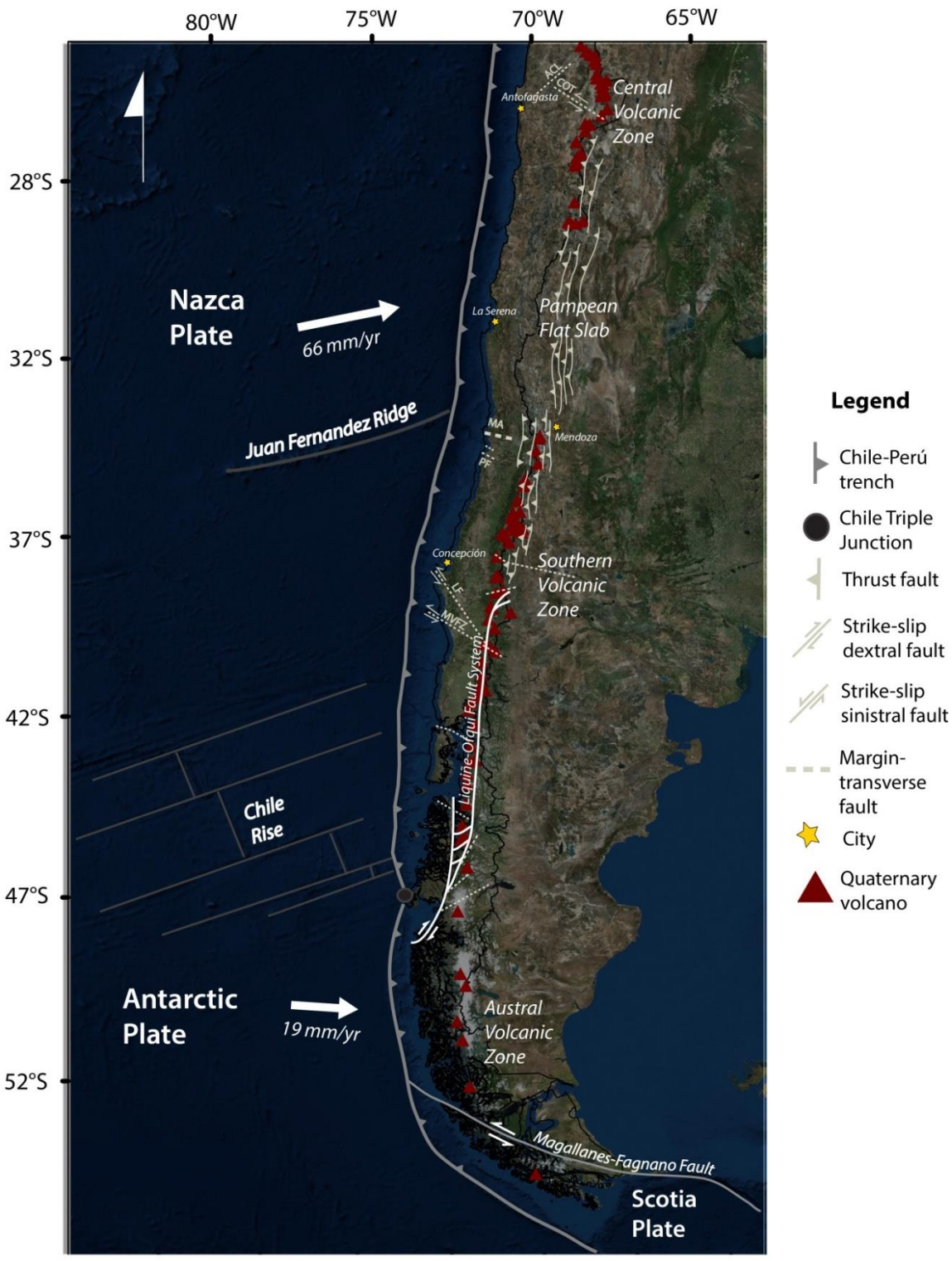
80°W
75°W
70°W
65°W
28°S
32°S
37°S
42°S
47°S
52°S
Nazca Plate
66 mm/yr
Antarctic Plate
19 mm/yr
Juan Fernandez Ridge
Chile Rise
Central Volcanic Zone
Pampean Flat Slab
Southern Volcanic Zone
Austral Volcanic Zone
Liquiñe-Ofqui Fault System
Magallanes-Fagnano Fault
Scotia Plate
Antofagasta
La Serena
Mendoza
Concepción
ACT
CDT
MA
PF
LF
MVFZ
Legend
Chile-Perú trench
Chile Triple Junction
Thrust fault
Strike-slip dextral fault
Strike-slip sinistral fault
Margin-transverse fault
City
Quaternary volcano

1.3 Statement of the problem

Obliquely convergent subduction margins commonly develop trench-parallel faults that shape the regional architecture of orogenic belts. Partitioning of interplate deformation is also commonly attributed to margin-parallel faults, which accommodate the trench-parallel component of deformation arising from oblique subduction. However, transverse faults also are common along most orogenic belts but have been largely neglected in strain partitioning analysis and orogen-building processes. It is then relevant to assess whether and how transverse faults accommodate plate-margin deformation arising from oblique subduction.

The SVZ constitutes an excellent area to address the above stated problem because it displays transverse-to-the-arc structures whose control in present-day volcanism is widely acknowledged. However, their tectonic role in terms of whether and how they accommodate crustal deformation arising from oblique subduction is poorly understood.

It has been proposed that the apparent paradox of misoriented crustal faults hosting volcanic complexes may be a consequence of the stress changes derived by the subduction seismic cycle [*e.g. Lara et al.,* 2004, 2006, 2008; *Sepúlveda et al.,* 2006]. During the coseismic phase of the SSC a geologically instantaneous (*i.e.* a duration of seconds to minutes) stress switch occurs due to the elastic rebound of the overriding plate [*Aron et al.,* 2013]. Then, misoriented faults with respect to the interseismic stress field should become optimally oriented to experience extension.

In this context, crustal discontinuities optimally oriented with respect to either the long-term stress field (*i.e*. during the interseismic period of the SSC) or a temporal stress field (coseismic stress field) may be activated and take up part of the deformation arising from oblique subduction. In consequence, to explore the relationship between the Andean subduction zone and faults within the upper plate is crucial to better understand

qualitatively and quantitatively how plate-boundary deformation is accommodated within the overriding plate.

This fundamental problem also has key implications regarding the assessment of geologic hazard associated with earthquakes resulting from the activation of crustal faults. Seismic hazard of crustal faults is commonly neglected in engineering codes and public policy in Chile, which only take into account subduction earthquakes [*e.g. Barrientos et al.*, 1990]. However, crustal earthquakes nucleate at very low depths (less than 20 km) making them largely destructive and dangerous (*e.g.* San Francisco 1906 Mw 7.8; Aysen 2007 Mw 6.2). The assessment of crustal earthquake hazard is thus a key issue that is currently being taken more into consideration [*e.g. Armijo et al.,* 2010], however, there is still much to add to the current knowledge of neotectonic activity due to crustal faulting.

1.4 Objectives

This research aims to unravel the tectonic role of margin-parallel and margin-transverse crustal faults in the accommodation of crustal deformation during oblique subduction at the Southern Volcanic Zone of the Andes. Specifics aims are: 1) To constrain the geometry, kinematics and slip rates of margin-parallel and margin-transverse faults during the interseismic phase of the subduction seismic cycle and 2) To determine the kinematics, slip distribution and normal traction distribution of margin-parallel and margin-transverse faults during the coseismic phase of the subduction seismic cycle.

To accomplish these objectives key case studies were selected of margin-parallel fault systems, the Liquiñe Ofqui Fault System (LOFS) and of NW-striking and ENE-striking structural domains within the SVZ. These were incorporated to a regional-scale numerical model using the Boundary Element Method to evaluate their elastic response during the different phases of the SSC.

1.5 Hypothesis

It is hypothesized that, although margin-parallel faults constitute the first-order elements responsible for orogen-building and strain-partitioning within obliquely subducting margins, transverse crustal faults play a significant contribution in accommodating plate-boundary deformation. It is therefore expected that the interseismic model will induce dextral-reverse kinematics at the margin-parallel LOFS accommodating a significant amount of the margin-parallel component of convergence. NW-striking faults are expected to display sinistral-reverse kinematics whereas NE-striking faults should display strike-slip dextral kinematics and should be optimally oriented to experience tensile stress due to the interseismic stress field, consistent with field evidence. Both structural domains should experience non-negligible slip rates close to one order of magnitude less than the LOFS.

The stress field induced by the coseismic phase of the SSC is expected to produce a switch in the kinematics at all the modeled faults. Margin-parallel faults become normal and NW-striking faults experience significant tension and normal-dextral kinematic whereas NE-striking faults become left-lateral and compressive due to this stress change. Therefore, transient stress changes through the SSC may explain the mechanism of magma transport on misoriented faults; however, it is hypothesized that the long-term structural grain at intra-arc faults will be dominated by the interseismic stress field.

1.6 Methodology: Theoretical background

The objectives of this research were addressed through a numerical modeling approach using the software Poly3D [*Thomas*, 1993]. In this section it is first described the theory behind the Displacement Discontinuity Boundary Element Method implemented in Poly3D. Secondly, a brief description on the use of dislocations to model fault

mechanics is presented followed by a description of how models in Poly3D are configured. Details on the model implementation are described in section 2.5 of this manuscript. The significance of the model implementation as well as the limitations arising from the assumptions and simplifications considered are discussed in section 2.6.4.

1.6.1 The Boundary Element Method of Displacement Discontinuity

Many complex problems in solid mechanics and other disciplines can be reduced to mathematical models known as boundary value problems. A partial differential equation models the physics of the problem in a region of interest *R*, which can be solved subject to constraints describing what happens on the boundary *C* of the domain. Analytical solutions to boundary value problems can sometimes be derived, however, for practical problems with complex geometries, heterogeneous materials and non-linear governing equations, analytical solutions often cannot be found. Solutions need then to be approximated using numerical methods.

The Boundary Element Method (BEM) is a widely used numerical technique for solving the partial differential equations governing a boundary value problem. With respect to other numerical techniques (*e.g* Finite Element Method, Finite Difference Method), this tool provides the advantage of only discretizing the boundary *C* instead of the entire domain *R*. The numerical solution builds on a singular analytical solution that has been obtained for each of the discretized elements of *C*, which combined satisfy the specified boundary conditions. The system of equations to be solved is thus much smaller than the system needed to solve the same boundary problem by the finite element method; however, the equations are not sparse because the solution on each element plays a part in every equation. Once these equations have been solved, the solution at any point in *R* can be constructed [*Crouch and Starfield*, 1983].

A particular BEM based formulation is the Displacement Discontinuity Method [*Steketee*, 1958; *Chinnery*, 1963; *Crouch and Starfield*, 1983], which has been widely used to solve problems in solid mechanics involving openings or cracks. This method is based on the 2D analytical solution to the problem of a constant discontinuity in displacement over a finite line within an infinite elastic solid [*Steketee*, 1958; *Crouch*, 1976a, b]. Physically, a displacement discontinuity may be regarded as a line crack whose opposing surfaces have been displaced relative to one another by a constant amount. If the crack is divided into *N* elements (boundary elements) each one with a constant displacement discontinuity, it is possible to obtain a discrete approximation to a continuous distribution of displacement along a crack.

A 2D curved crack can be represented by *N* straight elements each of which represent a displacement discontinuity (Figure 1-8). The discontinuity along the *j-th* segment of the line crack is defined by its components in shear D_s and normal D_n directions with respect to the local coordinate system *s* and *n*. The solution for the normal σ_n^i and shear σ_s^i stresses at the midpoint of the *i-th* element resulting from the combined displacement discontinuities on the *N* elements can be solved through the system of equations expressed in Equations 1-1 and 1-2. Influence coefficients $A_{ss}^{ij}, A_{sn}^{ij},$ etc, are derived from the analytical solution of the problem to relate displacements with stress [*Crouch*, 1976a, b], and depend mainly on the elasticity constants of the medium and the geometry of the elements.

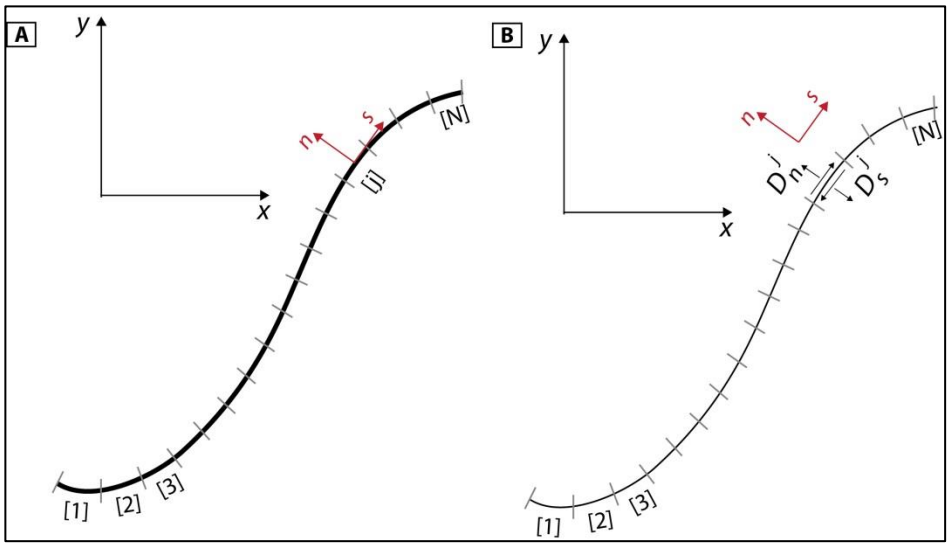

Figure 1-8. Representation of a 2D crack by N elemental displacement discontinuities. Modified after *Crouch and Starfield* (1983).

$$\sigma_s^i = \sum_{j=1}^{N} A_{ss}^{ij} D_s^j + \sum_{j=1}^{N} A_{sn}^{ij} D_n^j \quad Eq.1-1$$

$$\sigma_n^i = \sum_{j=1}^{N} A_{ns}^{ij} D_s^j + \sum_{j=1}^{N} A_{nn}^{ij} D_n^j \quad Eq.1-2$$

This problem can also be solved if the distribution of displacement along the crack is unknown, in which case the tractions σ_n^i and σ_s^i need to be specified for each element and the algebraic system is solved for the 2N equations for D_s^j and D_n^j. After this system is solved, the elastic response due to the combined displacement discontinuities can be computed anywhere in the surrounding elastic medium.

1.6.2 Poly3D: a BEM dislocation based program to study fault mechanics

Dislocation based methods have been one of the main tools used for mechanical faulting analysis for the past half century [*Maerten et al.*, 2014]. *Steketee* (1958a, b) proposed that Volterra's solution on the elastic fields produced by slip on an infinite edge dislocation within an elastic medium could be the proper tool to quantitatively describe the stress and displacement fields due to slip or opening across geologic structures. The notion is based on the idea that dislocations describe the part of elasticity theory dealing with surfaces across which the displacement components are discontinuous.

The dislocation based Displacement Discontinuity method described in the previous section, numerically solved through the Boundary Element Method, has been used to obtain solutions for 2D problems involving geologic structures [*e.g.Mavko*, 1982; *Delaney and Pollard*, 1981; *Olson and Pollard*, 1989, 1991], however, with this tool integration becomes lengthy and complicated even for 2D simple geometries.

The concept of angular dislocations, developed by *Burgers* (1939) and *Yoffe* (1960) was later used to overcome the issue of geometric limitations in dislocation based methods. An angular dislocation basically consists of the superposition of two dislocation lines that extend to infinity from a common vertex. *Comninou and Dundurs* (1975) solved the displacement field for an angular dislocation in an elastic half-space. This solution allowed constructing planar polygonal shaped elements of dislocations by the superposition of angular dislocations.

Thomas (1993) used the concept of polygonal dislocations to develop the C language code Poly3D. This software calculates the strain, stress and displacement fields produced by slip or opening at planar polygonal elements of displacement discontinuity in a whole or semi-infinite elastic medium. Geologically, a polygonal element may

represent some portion of a fracture or fault surface across which the discontinuity in displacement is approximately constant [*Maerten et al.* 2014]. Several superimposed triangular elements can be used to model geological structures with complex 3D boundaries and shapes (Figure 1-9).

Boundary conditions are prescribed on each element in its three local coordinates, which can be prescribed either as constant displacements, tractions or a combination of both (*e.g.* two local coordinates prescribed in tractions and one in displacement) (Figure 1-8). Remote strain or stress fields can also be prescribed as boundary conditions. Poly3D solves the three non-prescribed boundary conditions on each modeled element and calculates the elastic response due to the prescribed boundary conditions at any observation point located within the elastic medium.

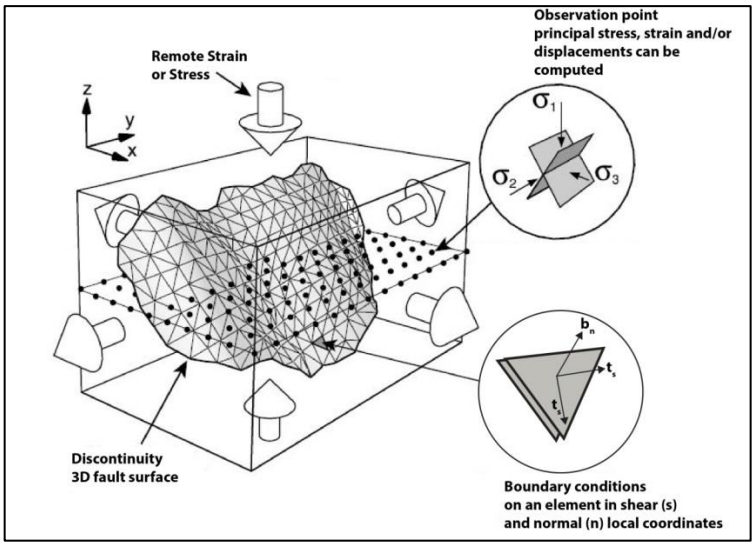

Figure 1-9. Example of a Poly3D model configuration. The discretization of a 3D fault surface into triangular boundary elements of displacement discontinuity allows the construction of a surface of any desired geometry. Boundary conditions can be applied remotely and locally, at the center of each element discontinuity. A case where the shear local coordinates are prescribed in traction boundary conditions and the normal coordinate is prescribed in displacement is shown. Observation points (black dots) can be prescribed anywhere within the elastic

medium, where displacement, strain and stress due to the prescribed boundary conditions can be computed. Modified after *Maerten et al*., (2002).

1.6.3. Elastic model of the Andean subduction zone

Poly3d was here used to implement a forward large-scale model of the deformation field in the upper crust due to the subduction at the Chilean margin during the interseismic and coseismic periods of the SSC. This method was selected because it provides the advantage of addressing the problem within a semi-infinite medium and only requiring the discretization of the boundary domains, which in this case represent crustal discontinuities. It is therefore possible to model the subduction process at a continental scale at a very low computational cost. Additionally, the elastic response due to the modeled boundary conditions can be calculated anywhere in the medium through the specification of observation points. This allowed verification of the displacement field computed by the model with GPS-measured displacement vectors (see Figure 2-5).

The interplay between motion of tectonic plates and slip in crustal faults was evaluated by including into the model case study faults representative of the main structural domains at the SVZ. The LOFS was selected as an emblematic case study of a major first-order margin-parallel fault system. Case studies representative of the second order transverse structures are the NW-striking Chillán-Cortaderas, an elongated N40°W-striking strato-volcano which continues to the east as a morphologic lineament [*Ramos and Folguera et al.* 2005] and the ENE-striking Callaqui-Copahue-Mandolegue Transference Zone [*Melnick et al.,* 2006] the alignment of two major strato-volcanoes, minor eruptive centers and eroded calderas. These two features are believed to be the surface manifestation of deep-seated faults acting as magma-feeders for the volcanic complexes emplaced on them.

The selected case studies were included into the BEM model to evaluate their slip sense and slip rate during the interseismic and coseismic stages of the SSC. They were

implemented as free-slipping crustal discontinuities, with their observed surface geometry and inferred geometry in depth.

By including the faults as pre-existent discontinuities in the medium it becomes reasonable to consider certain simplifications of the complexity of the regional scale tectonic problem addressed here. First, the nature and driven mechanism that originated the case study faults is still an ongoing debate. On a lithospheric scale, the location of a strike-slip fault is partially controlled by thermal weakening of the intra-arc lithosphere resulting from upward movement of magmas [*De Saint Blanquat et al*., 1998]. This mechanical weakening favors shear localization and formation of strike-slip faults [*e.g. Holford et al.*, 2011]. However, by implementing pre-existent discontinuities, shear is forced to localize on the fault, thus to neglect rheological changes due to thermal weakening is a reasonable simplification. Also, the debate on the driven mechanism causing slip on the LOFS (Rise collision and/or oblique subduction) is not considered in this study because the focus is to address the mechanical interaction between oblique subduction and crustal faulting. In consequence, results from this study may reflect some differences with respect to geological observations, which would imply that oblique subduction is not the only mechanism driving crustal deformation.

1.7. Main results

A brief description of the main outcomes of this research is presented in this section. The detailed results are presented and discussed in sections 2.5 and 2.6 of this manuscript.

Result provided by the interseismic model show that the LOFS displays oblique slip, with dextra-reverse sense of slip at a rate of 1-7 mm/yr with a decreasing gradient towards the north. The NW-striking Chillán-Cortaderas (ChC) shows reverse-sinistral

slip sense with a minimum slip rate of 0.4 mm/yr in its eastern portion and a maximum of 1.4 mm/yr localized in its western termination. The ENE-striking Callaqui-Copahue-Mandolegue (CCM) shows purely strike-slip dextral kinematics all across the fault at a maximum rate of 0.85 mm/yr. Normal traction distribution at this fault shows that ENE striking faults experience normal tension, which favors fluid and magma ascent through them during the interseismic period of the SSC. On the contrary, the ChC exhibits compressional normal tractions during the interseismic, obstructing fluid migration. The coseismic simulation exhibits that all modeled faults switch their sense of slip as a result of this stress regime. In this scenario, NW-striking faults experiences normal tension at a maximum of 0.6 MPa, located right below the Nevados de Chillán volcanic complex.

By considering the slip rates obtained from this study, a first-order approximation of the magnitude of maximum crustal earthquake that could be nucleated at the case study faults can be computed. Earthquakes with magnitudes ranging from Mw 6.27 to 6.93 should be expected at the LOFS, whereas the maximum earthquake that could occur at the ChC and CCM are of Mw 6.66 and 6.77, respectively.

1.8. Conclusions and future perspectives

The conclusions of this research are listed in section 2.7, here the main contributions of this manuscript and future perspectives are presented. First, the implementation of this forward continental-scale model, which was verified with GPS surface deformation, constitutes a new methodology to evaluate the elastic response of crustal faults within any region of the Andes to tectonic plate motion. This is a significant contribution because field data from geological faults is extremely limited and by means of this method, the first-order behavior of faults can be constrained.

Secondly, this research shows that margin-transverse faults respond significantly to slip at the subduction zone, which suggests that they play a significant contribution in the

accommodation of crustal deformation arising from oblique subduction. As a result, the current paradigm where slip partitioning of oblique subduction is exclusively accommodated at margin-parallel faults is challenged.

Third, the response of crustal faults to the tectonic regime of the coseismic phase of the SSC is to switch their sense of slip, as shown in the implemented model. The implications of this are significant because it shows that faults with orientations favoring a compressive behavior during the interseismic are subjected to significant tension during the coseismic, which could be driven mechanism for magma feeding for volcanic complexes emplaced on them. Finally, this approach allows constraining maximum crustal earthquakes at modeled faults, which has significant impacts in the estimation of seismic hazard associated with crustal faulting.

This research should be complemented in the future with further field studies on the case study faults and other intra-arc faults within the SVZ. These should include geological and structural mapping and geophysical surveys to better constrain the depth geometry of intra-arc faults. Additionally, some of the variables of this complex problem could be taken into account in a less simplified model. These should include rock anisotropy, rheological changes due to thermal anomalies, viscous-elastic behavior of the upper crust and plastic deformation mechanisms at depth.

2. TECTONIC ROLE OF MARGIN-PARALLEL AND MARGIN-TRANSVERSE FAULTS DURING OBLIQUE SUBDUCTION AT THE SOUTHERN VOLCANIC ZONE OF THE ANDES: INSIGHTS FROM BOUNDARY ELEMENT MODELING. (Article submitted to *Tectonics*)

2.1 Introduction

Major crustal faults and fold systems at convergent margins are commonly organized into margin-parallel, high-strain domains that shape the first-order architecture of orogenic belts. However, second-order, oblique-to-the-orogen structures can also be found within the overall margin-parallel structural grain that characterize convergent margins. Regional scale transverse structures have been documented along the length of the Andes [*e.g.Katz* 1971; *Melnick and Echtler*, 2006; *Glodny et al.*, 2008] which cut the well-organized N-S architecture of the Central and Southern Andean orogen.

These transverse structures have been recognized as: 1) NW-trending major magnetic and gravimetric anomalies [*Yañez et al*., 1998], 2) NW and NE-striking long-lived faults spatially and genetically associated with porphyry copper deposits [*Mpodozis and Cornejo*, 2012; *Piquer et al.*, 2015], 3) ENE and NW-trending alignments of major strato-volcanoes and minor eruptive vents within the intra-arc [*e.g. Cembrano and Moreno*, 1994, *López-Escobar et al.* 1995] and 4) NW-trending morphologic lineaments in the fore-arc that recent structural and seismological data have associated with neotectonic activity [*e.g. Haberland et al.*, 2006; *Farías et al.*, 2011].

Geophysical and geological evidence on these Andean Transverse Faults (ATF) suggests that some of them are long-lived lithospheric-scale features [*Yañez et al.*, 1998; *Yañez and Cembrano*, 2004] associated with seismic segmentation of the plates interface [*Melnick et al.*, 2009], enhanced rock damage, past and present fluid flow and ore deposit clustering [*e.g. Chernicoff et al.*, 2001; *Sánchez et al.*, 2013]. Within the intra-

arc, the ATF exert a fundamental structural control on Quaternary volcanism in the Central and Southern Andes [*Tibaldi et al.*, 2005; *Lara et al.*, 2006; *Melnick et al.*, 2006; *Acocella and Funiciello*, 2009; *Cembrano and Lara*, 2009]. Despite the widely acknowledged relevance of ATF in controlling subduction-related processes, their tectonic role in terms of whether and how they participate in the accommodation of crustal deformation is still poorly understood.

Within subduction margins displaying oblique convergence, the trench-parallel component of deformation can be accommodated within the upper plate as a result of the partitioning of interplate slip [*Fitch*, 1972; *Jarrard*, 1986a, 1986b; *Beck*, 1991; *Tikoff and Teyssier*, 1994]. Strain partitioning arising from oblique subduction is typically attributed to margin-parallel strike-slip crustal faults, *e.g.* Sumatra [*Fitch*, 1972], Eastern Turkey [*Jackson, 1992*], New Zealand [*Cashman et al.*, 1992]. Margin-transverse faults, however, have been largely neglected, hampering a full understanding of continental margin strain partitioning.

Crustal discontinuities or inherited fault zones favorably-oriented with respect to the long-term, secular stress field (*i.e.* the interseismic period of the SSC) and/or a short-term stress field (coseismic period) may activate and take up part of the deformation within the overriding plate, typically associated with margin-parallel structures. Therefore constraining the kinematics and estimated slip rates of differently-oriented crustal faults could greatly improve the understanding of how deformation due to oblique subduction is partitioned at crustal faults.

The Boundary Element Method (BEM) [*Crouch and Starfield*, 1983] using polygonal dislocation elements [*Comninou and Dundurs*, 1975] of displacement discontinuity is one of the most versatile and widely-used numerical techniques to solve problems involving fractures at an elastic medium because it allows modeling complex geometries of fault surfaces without gaps or singularities and at a relatively low computational cost.

We implement a forward 3D BEM model of subduction at the Chilean margin using Poly3D[*Thomas,* 1993] to simulate the deformation field in the upper plate during different stages of the SSC. Our goal is to evaluate the elastic response of crustal faults to constrain their kinematics and potential slip rates during the individual phases of the SSC. To accomplish this, we select key case studies of margin-parallel and margin-transverse structures within a particular region of the Andes, the Southern Volcanic Zone (SVZ), which constitutes the intra-arc region of the Southern Andes (Figure 2-1).

Results confirm our hypothesis that the partitioning of slip at obliquely convergent margins is a more complex process than previously recognized: many crustal faults with various orientations play a significant role in the accommodation of crustal deformation. This process can be strongly influenced by the temporally variable stress regimes associated with individual phases of the SSC. Our results have a great impact on the estimation of geologic hazard arising from intraplate earthquakes at margin-parallel and margin-transverse faults. Additionally, the model implementation used here constitutes a new methodology that can be further used to evaluate first-order response of previously constrained fault geometries within any region of the Andes.

2.2 Tectonic setting

The Southern Volcanic Zone (SVZ) (Figure 2-1) makes up the volcanic arc of the Southern Andes between latitudes 33°S and 47°S. This region has undergone major megathrust earthquakes (e.g. Mw 9.5, Valdivia 1960; Mw 8.8 Maule 2010) resulting from the oblique subduction of the Nazca plate underneath the South American plate at a rate of 66 mm/yr [*Angermann et al.*, 1999].

The SVZ displays remarkable along-strike structural variations. The northern portion (33°S-38°S) is characterized by well-developed margin-parallel fold and thrust belts,

and a high (up to 6.9 km) and wide (up to 800 km) main Cordillera. No surface-trace of a strike-slip fault system is recognized in the area; however, seismic data of shallow crustal earthquakes displaying right-lateral kinematics within the intra-arc [*Farias et al.*, 2006] suggests that some strain-partitioning is occurring at depth.

The Patagonian Andes (38°S-47°S), in turn, are characterized by a low (up to 3.5 km) and narrow Cordillera mainly consisting of major strato-volcanoes. This area is structurally dominated by the 1200 km long, strike-slip, Liquiñe-Ofqui Fault System (LOFS) [*Hervé,*1976; *Hervé*, 1994; *Cembrano et al.*, 1996]. Evidence of dextral slip of the LOFS since the Pliocene [*Cembrano et al.*, 2000] suggests a partitioned tectonic regime where the upper plate accommodates part of the margin-parallel component of deformation arising from oblique subduction. Transpressive tectonics characterizes the area with NE-trending, subhorizontal $\sigma_1$and subvertical σ_2[*Lavenu and Cembrano*, 1999].

Strato-volcanic complexes, minor eruptive centers and geothermal springs within the SVZ are roughly aligned and appear to be emplaced on top of morpho-structural lineaments, representing second-order structures within the intra-arc (Figure 2-1). Two categories of these second-order morpho-tectonic features are recognized within the SVZ [*López-Escobar et al.*, 1995; *Cembrano and Lara*, 2009; *Melnick et al.*, 2006]: (1) NE striking faults favorably oriented for dextral shear sense along with ENE arc-oblique transtensional subsidiary faults (*e.g.* Callaqui-Copahue-Mandolegue, Sollipulli strato-volcano, Osorno-Puntiagudo volcanic alignment) and (2) NW to WNW-striking features, which are misoriented with respect to the prevailing secular stress field to promote magma ascent through the lithosphere. Examples of these structures are the Nevados de Chillán volcanic complex, the Villarrica-Quetrupillán-Lanin volcanic chain (spatially associated with the Mocha-Villarrica Fault Zone [*Melnick and Echtler*, 2006]), the Cordon Caulle volcanic complex [*Sepúlveda et al.*, 2005; *Lara et al.*, 2006] and the Chaiten strato-volcano. These eruptive centers are thought to be the surface

manifestation of deep seated structures associated with long-lived fault systems that currently represent crustal discontinuities acting as episodic magma pathways through the lithosphere [*Cembrano and Moreno*, 1994; *Cembrano and Lara*, 2009; *Pérez-Flores et al.*, 2016].

It has been proposed that the seismic cycle of subduction (SSC) plays a fundamental role in the time-dependent nature of these pathways [*Lara et al.*, 2006]. Crustal relaxation during elastic rebound produced by a megathrust event induces a quasi-instantaneous inversion of the stress field. In this circumstance, misoriented structures become optimally oriented to geologically-instantaneous extension promoting magma ascent.

Despite the widely acknowledged relevance of arc-oblique structures, their exact geometry, kinematics and estimated slip rates are still poorly constrained by geological observation. This is a result of very limited exposure of outcrops generally covered by thick vegetation, difficult access due to rugged terrain, high erosion rates and lack of regional/local geophysical surveys. Consequently, to better understand the tectonic role of margin-parallel and margin-transverse structures, we have selected representative case studies from the SVZ to be incorporated into a regional scale numerical model. These are the margin-parallel LOFS, the ENE-striking Callaqui-Copahue-Mandolegue Transference Zone (CCM) and the WNW-striking Chillan-Cortaderas Lineament (ChC) (Figure 2-1).

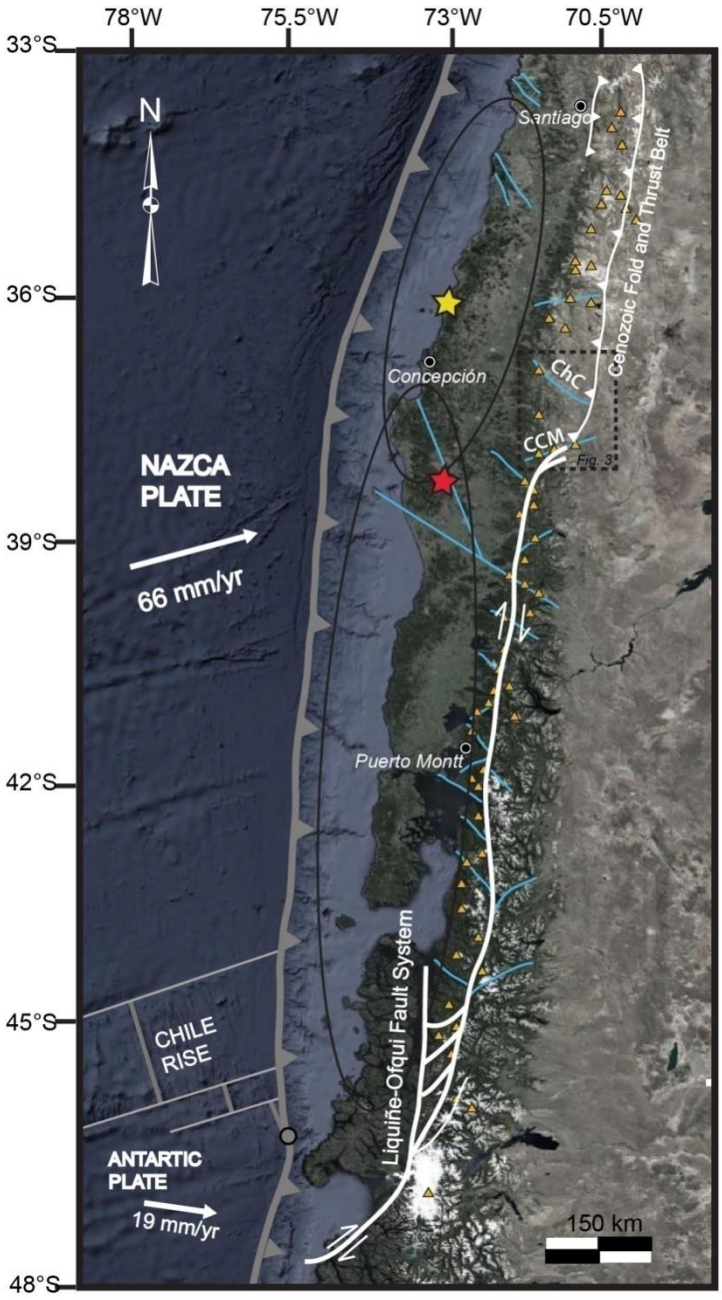

Figure 2-1. Southern Volcanic Zone of the Andes; quaternary volcanoes are shown in yellow. Major margin-parallel fault systems are displayed in white whereas transverse faults are shown in blue. Yellow and red stars represent the epicenters of Maule 2010 and Valdivia 1960 megathrust earthquakes, respectively. Approximate rupture zones associated with these two events are shown in black ellipses. The ATF selected as case studies are the NW-striking Chillán-Cortaderas (ChC) and the ENE-striking Callaqui-Copahue-Mandolegue (CCM). The rectangle in dashed lines represents the area shown in Figure 2-3.

2.3 Case studies

2.3.1 The Liquiñe-Ofqui Fault System

The LOFS is a 1200 km long, intra-arc fault system constituting the longest active strike-slip fault within the Andes. The LOFS consists of two NNE-striking branches hundreds of kilometers long, referred to as Eastern and Western master faults in this work (Figure 2-2). They are arranged in a duplex-like geometry, joined by NE-striking *en echelon* faults tens of kilometers long forming the duplex [*Cembrano et al.*, 1996] (Figures 1 and 2). Evidence of dextral slip along the LOFS at least since the Pliocene [*Cembrano et al.*, 2000] is attributed to strain partitioning resulting from oblique convergence between the Nazca and South American plates during the past 48 my [*Pardo-Casas and Molnar*, 1987]. Other authors have suggested that dextral displacement along the LOFS and northward motion of the fore-arc sliver developed west of the fault (also called Chiloé Block, Figure 2) is accentuated and even driven by the subduction of the active Chile Rise at 47°S (Figure 1) since the middle Miocene [*Forsythe and Nelson*, 1985; *Murdie et al.*, 1993; *Thomson*, 2002].

The exact geometry and depth extent of the LOFS remains unclear due to limited data. However, a regional-scale geometry can be obtained from the following sources: (1) compilation of surface-traces of the LOFS mapped and inferred by previous authors [*Hervé et al.*, 1994; *Cembrano et al.*, 1996; *Pérez-Flores et al.*, 2016] (2) published and unpublished fault slip data of brittle deformation associated with the LOFS and fault plane solutions [*Cembrano et al.*, 2000; *Vargas et al.*, 2013; *Pérez-Flores et al.*, 2016] (3) shallow earthquakes hypocenters and focal mechanisms [*Chinn and Isacks*, 1983; *Dziewonski et al.*, 1990, 1999, *Lange et al.*, 2008; Global CMT Catalog] and (4) location of quaternary volcanoes and minor eruptive vents [*López-Escobar et al.*, 1995]. According to these geological and seismic data (Figure 2), the Eastern master trace dips steeply to the west (~80°) and displays dextral kinematics. Less information is available

with respect to the Western master trace of the LOFS because of extremely difficult access; however, evidence of uplifted blocks within the duplex formed by the two master faults [*Thomson*, 2002; *Vargas et al.*, 2013] suggests that this branch dips steeply to the east, displaying dextral-reverse kinematics.

The depth of shallow focal mechanisms associated with the LOFS proves that this fault system extends to a depth of at least 15-20 km [*Lange et al.*, 2008]. This observation is corroborated by the presence of exhumed mylonitic outcrops along the LOFS that display an internal structure consistent with the overall kinematics and age of the LOFS [*Cembrano et al.*, 2000], suggesting that this fault extends beyond the brittle--plastic transition. Furthermore, a number of volcanoes (*e.g.* Mochos-Chosuenco) and monogenetic cones are located along the LOFS surface-trace [*Lara et al.*, 2008], many of which display a very primitive signature (*e.g.* Caburgua, Ralún-Cayutué, Puyuhuapi) which suggests that this fault may constitute a direct magma pathway from the asthenosphere [*Cembrano and Lara*, 2009]. This hypothesis is consistent with a model in which the LOFS decouples the lithosphere and the block west of the fault (Chiloé Block) becomes a fore-arc sliver with northward motion [*Beck et al.*, 1993; *Lavenu and Cembrano*, 1999; *Rosenau et al.*, 2006; *Wang et al.*, 2007].

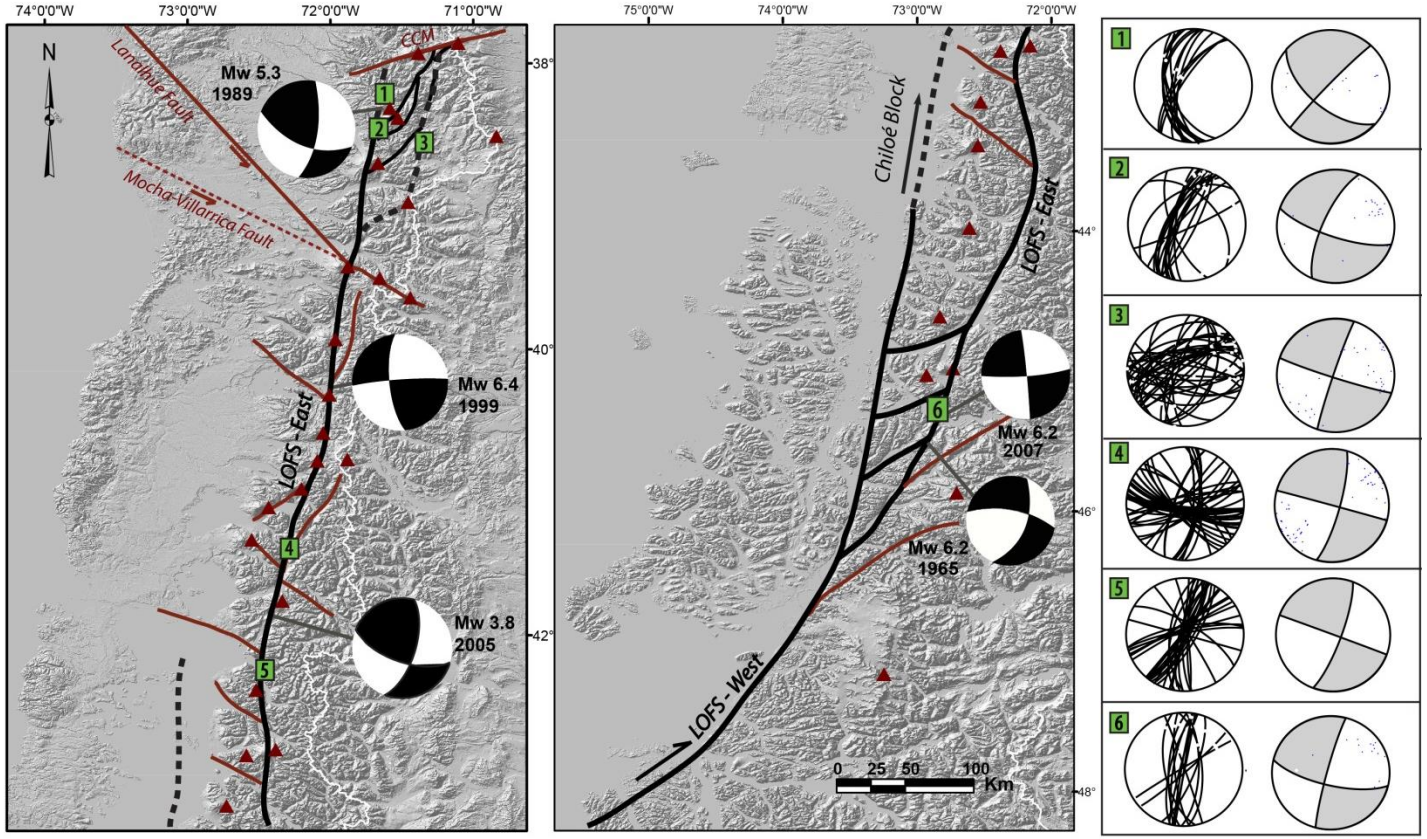

Figure 2-2. Compilation of mapped (black) and inferred (dashed black) traces of the LOFS, subsidiary faults and oblique-to-the-arc (red) morpho-tectonic associations within the SVZ [*Hervé et al.*, 1994; *Cembrano et al.*, 1996; *Vargas et al.*, 2013; *Pérez-Flores et al.*, 2014]. Shallow focal mechanisms of crustal seismicity associated with the LOFS [*Chinn and Isacks*, 1983; *Dziewonski et al.* 1990, 1999; *Lange et al.*, 2008; Global CMT Catalog] are shown. Evidence of brittle deformation related to the LOFS has been found at the six structural sites shown. Lower hemisphere projections of published [*Cembrano et al.*, 2000; *Vargas et al.*, 2013; *Pérez-Flores et al.*, 2016] and unpublished (sites 1 and 5) fault slip data with their corresponding fault plane solution and P axis.

2.3.2 NW-striking structural domains: The Chillán-Cortaderas Lineament as a case study

The Nevados de Chillán volcanic complex located at 36.9°S (Figure 2-3) is an elongated N40°W-trending volcanic chain comprising two andesitic to dacitic sub complexes separated by numerous cones and craters [*Dixon et al.,* 1999]. Its most recent eruption occurred in 2003, but during 2015 and 2016 preventive alerts has been established due to intense fumarolic activity.

The trend of this elongated volcanic complex appears to be inconsistent with the ~N70°E trend of σ_1 calculated for the region [*Lavenu and Cembrano,* 1999]. For this reason the Nevados de Chillán volcanic complex was selected as a case study representative of the NW-striking ATF which are misoriented with the regional stress field to promote magma ascent through the lithosphere.

The Nevados de Chillán volcanic complex appears to be the continuation to the west of a major morphologic lineament, the ~N70°W Cortaderas Lineament (CL), which runs for approximately 200 kilometers, from the main Cordillera in Chile toward the foreland in Argentina. Previous studies emphasize the role of the CL in the long and short-term tectonics and magmatism of the Andean arc and back-arcregion since at least thePaleocene[*Ramos and Barbieri*, 1989; *Ramos and Folguera*, 2005]. The Chillán-Cortaderas (ChC) has also been interpreted to be a structural accommodation zone allowing the balance of deformation between Oligo-Miocene sub-basins[*Radic*, 2010].Unfortunately, other than the surface-trace of this lineament, there is no further information regarding its nature or depth geometry. In this work it is interpreted to be a crustal discontinuity, with potential for accommodating slip.

2.3.3 ENE-striking structural domains: The Callaqui-Copahue-Mandolegue Transference Zone as a case study

The Callaqui-Copahue-Mandolegue (CCM), (Figure 3) is a 90 km long, N60°E trending volcanic chain [Melnick et al., 2006] that is genetically linked with a concealed, ENE-striking dextral transfer fault. The CCM consists of: (1) The basaltic to andesitic Callaqui strato-volcano, and related 15 km long, fissure shaped by the alignment of numerous vents and dikes; (2) The Copahue strato-volcano and (3) The Cordillera de Mandolegue, a 40 km long alignment of collapsed strato-volcanoes and minor eruptive centers.

The CCM orientation is sub-parallel to the regional trend of σ_1, which results in a favorable orientation to promote extension and magma ascent through the lithosphere [*Nakamura et al.,* 1977]. This is consistent with the alignment of hundreds of dikes with similar strike mapped along the Callaqui volcano fissure [*Sielfeld et al.,* 2016]. The CCM is located directly north of the northern termination of the LOFS and is thought to decouple the active deformation between the back-arc Antiñir-Copahue thrust fault zone to the north, and the LOFS to the south [*Folguera et al.,* 2004] (Figure 3-3). Local transtensional tectonics governs the northern termination of the LOFS [*Potent,* 2003], and evidence of dextral shear has been found within the Callaqui volcano [*Sielfeld et al.,* 2016]. The CCM was selected as a case study to represent the ENE-striking ATF within the SVZ.

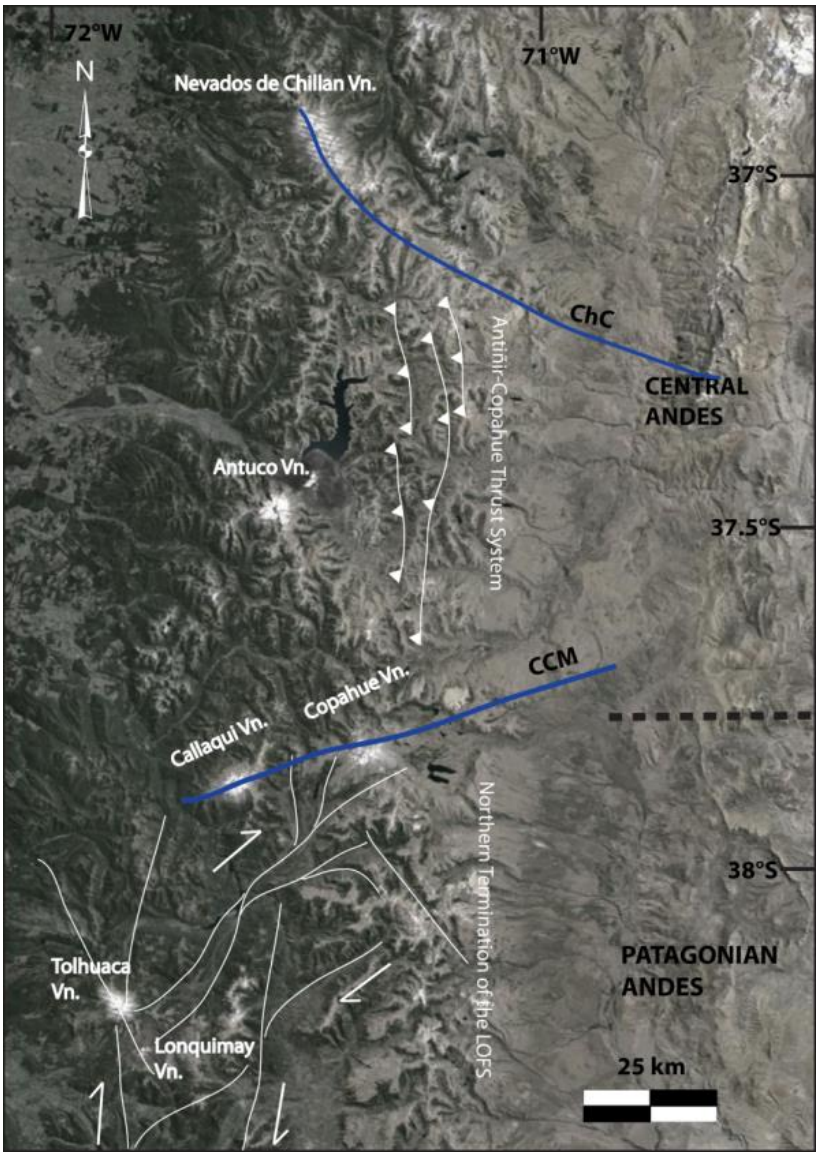

Figure 2-3. Transitional Zone between Central Andes and Patagonian Andes at the SVZ. In white lines are shown the main traces of the Northern termination of the LOFS (Perez-Flores et al. 2016) and the Antiñir-Copahue Thrust System (Folguera et al., 2004). In blue are displayed the transverse structures selected in this work for case studies: the NW-striking Chillan-Cortaderas Lineament (ChC) and the NE-striking Callaqui-Copahue-Mandolegue Transference Zone (CCM).

2.4 Methodology

2.4.1 Boundary Element Method

We study the mechanical interaction between slip in the subduction zone and faults in the overriding plate using the BEM code Poly3D[*Thomas*, 1993; *Maerten et al.*, 2014]. With this tool, faults and other types of geologic discontinuities are represented by discretized surfaces composed of triangular constant displacement discontinuity elements. Three boundary conditions of tractions and/or displacements are prescribed on each triangular element in a local coordinate system and Poly3D solves the linear elastic equations for the other three displacement or tractions on all the elements and for the stresses and displacements throughout the model domain.

Here we use Poly3D to implement a large-scale forward model of the deformation field in the upper crust due to the subduction at the Chilean margin during the interseismic and coseismic periods of the SSC. Once the model was implemented and constrained with geological and GPS-derived information, we incorporate the selected case study structures as meshed fault surfaces, which allow for determination of kinematics and estimated fault slip rates during the different stages of the SSC.

2.4.2 Subduction model: Interseismic phase set up

We model the subduction of the Nazca plate underneath the South American plate at the Chilean margin as an elastic, quasi-static process at a semi-infinite, faulted but otherwise isotropic, half space. The model domain includes the latitudinal range between 28°S and 47°S, which encompasses the study area (36°S-47°S) with an extension to the north that allows verification with more data and reduces the effect that the border of the model could produce in the calculated crustal deformation. We simulate the deformation field in the continental crust during the interseismic period of the SSC by introducing two

surfaces to the elastic medium: one representing the base of the oceanic lithosphere (Figure 2-4.a,b), and a second surface representing the megathrust interface between the subducting Nazca Plate and the overriding South American Plate (Figure 4.a,c). The geometry of the plate interface is based on the Slab 1.0 model [*Hayes et al.*, 2012] and was discretized into 1024 triangular elements. The detachment surface representing the base of the oceanic lithosphere was discretized into 3757 triangular elements and consists of a 1000 km wide flat surface located at 50 km depth and a subducting portion to the east with a geometry that mimics the plate interface.

In more traditional modeling exercises using Poly3D, stresses or strains are prescribed in the far field, and these drive slip and deformation around the model faults [*Maerten et al.*, 2002; *Griffith and Cooke*, 2004, 2005]. Because of the expected complexity of the regional stress state expected over the scale of our model, this is an unrealistic loading scenario. Instead, we adopt an approach similar to that of *Dair and Cooke* (2009) and*Marshall et al.*(2008) and loaded faults in the upper crust (LOFS, ChC and CCM) by prescribing slip on a detachment surface at the base of the oceanic lithosphere.

Interseismic deformation is typically simulated using a back slip approach [*e.g. Savage et al.*, 1983; *Bevis and Martel*, 2001] whereby reversing the coseismic slip on the locked portion of the fault mimics the interseismic deformation field. We chose boundary conditions differently in a way that the induced deformation field is controlled directlyby the long term plate convergence vector. The prescribed local boundary conditions on the model surfaces in order to simulate secular (*i.e.*, long term interseismic) deformation are shown in Figure 2-4. Normal displacements for all elements are equal to zero (no opening or penetration). Shear displacement discontinuity prescribed along elements in the flat portion of the detachment surface (Figure 2-4.b) are prescribed such that two shear displacement components sum to the convergence vector [*Angermann et al.*, 1999; *Kendrick et al.*, 2003] whereas elements in the dipping part of this surface are traction-free, representing a weak fault that creeps in response to

horizontal motion of the oceanic plate. On the subduction interface (Figure 2-4.c), elements located above 45 km depth are locked (not allowed to slip), simulating the seismogenic zone [*e.g.Bevis and Martel*, 2001]. Elements within deeper portions of the slab are traction-free and slip in response to loads associated with motion elsewhere in the model. While these boundary conditions do not include complex interseismic locking rate distributions within the seismogenic portion of the plate interface [*e.g.Moreno et al.*, 2012], we are focused on simulating long-term deformation equivalent to several seismic cycles, so we do expect this to generate some discrepancies when compared to crustal deformation data from the current interseismic period.

The prescribed boundary conditions induce a down-dip motion of the elastic medium located between the two surfaces, resulting in reverse slip on the subducting plate interface. Because the modeling tool is quasi-static, the time of simulation is arbitrary. Results presented here are divided by the years of simulation, representing velocity fields or slip rates. The elastic medium is assumed to have a Young's modulus of 120 GPa, representative of the continental crust [*Wang et al.*, 2007] and a Poisson ratio of 0.25.

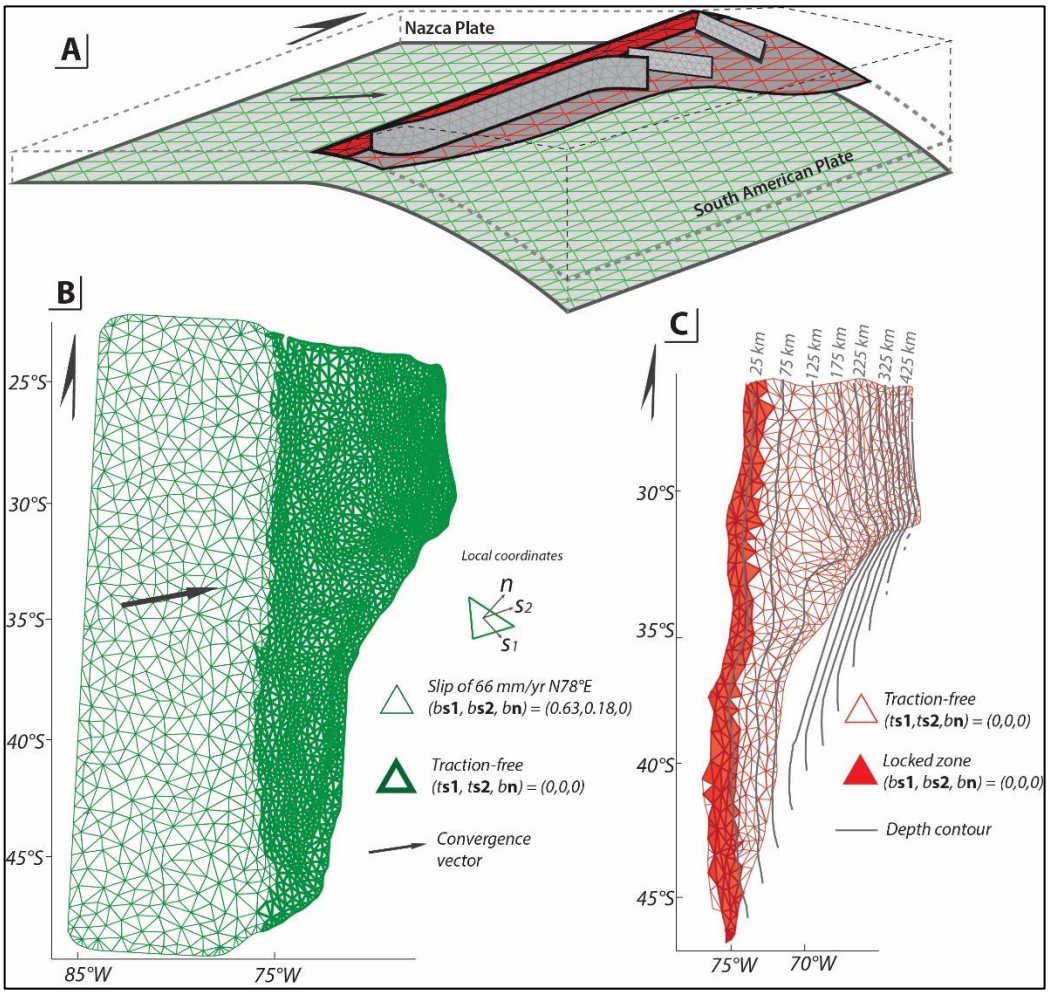

Figure 2-4. Implementation of the interseismic phase model. A) Schematic illustration showing the surfaces used to implement this model: the detachment surface representing the base of the Nazca plate (green) and the plate interface (red) with the seismogenic zone in filled red. Margin-parallel and margin-transverse crustal faults to be incorporated in the model are shown for reference. B) Geometry and boundary conditions on the base of the oceanic lithosphere. C) Geometry and boundary conditions on the plates interface [*Hayes et al.*, 2012].

To verify that the model geometry and boundary conditions provide a first-order simulation of secular crustal deformation fields in the study area, computed surface velocities were compared to GPS-derived velocity vectors (Figure 5). A total of 118 data points from multiple campaigns [*Wang et al.*, 2007; *Ruegg et al.*, 2009; *Moreno et al.*, 2011; *Lin et al.*, 2013] with their corresponding uncertainties were considered in this

analysis. These data points represent velocity of deformation, with respect to stable South America, during an interseismic phase of the subduction seismic cycle (1996 – 2009) and spanning a latitudinal range from 26°S to 45°S.

The misfit in magnitude between the velocity vector calculated by the model (v_{model}) and the GPS-derived vector (v_{GPS}) for each point in the data set was calculated using Equation 2-1; misfit contours are shown in Figure 2-5.

$$e = \frac{|v_{model} - v_{GPS}|}{v_{GPS}} * 100 \quad (Equation\ 2-1)$$

Because in this first implementation the model considers a non-faulted isotropic crust, results predict an overall non-partitioned tectonic setting. As a result, excellent fit (error between 0% and 20%) is obtained for the data points located between 27°S and 33°S, where geological evidence suggests that strain-partitioning is not occurring [*Hoffmann-Rothe et al.*, 2006]. South of 36°S the misfit increases to 20-40% which is consistent with abundant evidence of strain-partitioning occurring in the area [*e.g. Lavenu and Cembrano,* 1999]. Particularly large errors are concentrated west of the LOFS at 43°S where the northward motion of the sliver (Chiloé Block) obtained by GPS data [*Wang et al.*, 2007] are not predicted by the model implementation. Additionally, GPS vectors in the southern region are characterized by heterogeneity in terms of magnitude and direction, which suggests that local stress perturbations disturbed the regional deformation pattern at the time of the measurements. This can result from variable locking distribution, inherited stress heterogeneity, crustal faulting and/or post-seismic relaxation. Misfit magnitudes all along the model domain increase inland, where also GPS data points display considerably larger uncertainties.

Although local and temporal heterogeneities are not reflected by the model, the overall magnitude and distribution of the misfit suggests that this approach is suitable for

modeling long-term deformation at a regional scale, which is the purpose of this work. Consequently, results in terms of kinematics and magnitude of slip for crustal faults can be considered as reasonable estimations for the long-term deformation within the upper crust.

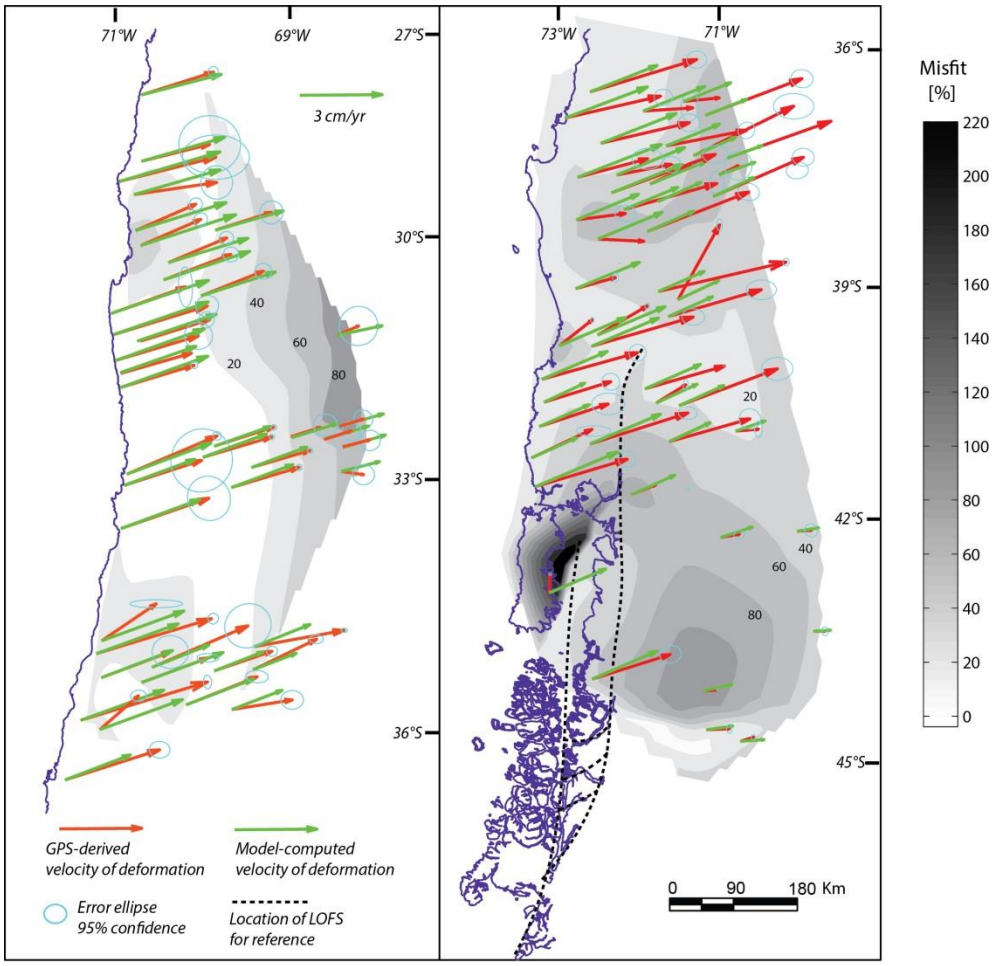

Figure 2-5. Interseismic GPS-derived velocity vectors [*Wang et al.*, 2007; *Ruegg et al.*, 2009; *Moreno et al.*, 2011; *Lin et al.*, 2013] compared to model-computed vectors. Misfit contours are shown in grayscale with corresponding colorbar. Computed deformation, GPS-derived deformation, misfit in magnitude and angular misfit for each site of the data set is available in table S1 of Supplementary Material. The approximate location of the LOFS is shown in dashed lines for reference (this first model does not include the LOFS or any other crustal fault).

2.4.3 Subduction model: Coseismic phase set up

We also simulated the coseismic phase of the SSC due to the 2010 Maule Mw 8.8 earthquake, which ruptured a segment of ca. 600 km, between Valparaiso and the Arauco Peninsula (Figure 1). Our goal was to model the deformation field induced in the upper crust during this event to evaluate its effect on crustal discontinuities. The Maule earthquake is the largest event at this plate boundary to rupture a mature seismic gap in an area that was geodetically monitored before and after its rupture. Abundant data from multiple GPS networks allowed for a higher resolution inversion of the slip distribution at the plate interface during this megathrust event [*Vigny et al.*, 2011; *Moreno et al.*, 2012]. We used the slip distribution and fault model by [*Moreno et al.*, 2012] (Figure 2-6) to prescribe the slip distribution on the elements of the plate interface located within the rupture zone of this earthquake.

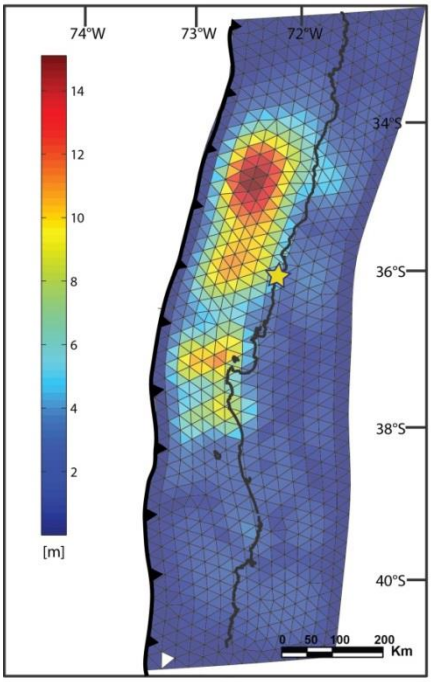

Figure 2-6. Map view of the plate's interface within the rupture area of the Maule earthquake, with coast line for reference. Colors show slip (in meters) prescribed on each triangular element to model the deformation field induced by the Maule 2010 megathrust earthquake, as obtained by [*Moreno et al.*, 2012]. Star indicaste location of the epicenter of theevent.

2.4.4. Case studies implementation

We implemented the three chosen case study structures (Figures 2-1, 2-2 and 2-3) in the upper plate as additional discretized surfaces, and we studied their mechanical behavior under both interseismic and coseismic boundary conditions. These surfaces represent crustal discontinuities with the potential of accommodating slip and facilitating crustal deformation. We model all of the case structures as freely slipping discontinuities.Although some frictional resistance to sliding is expected for natural faults, this is a suitable first order approach to model the long-term slip at crustal faults (creeping plus coseismic slip through the seismic cycle of individual faults) [*Dair and Cooke*, 2009]. Although this approach is appropriate for interseismic long-term deformation, to consider free-slip on surfaces under the quasi-instantaneous deformation field due to the coseismic phase of the SSC may lead to overestimations of slip. Consequently, the significance of coseismic results is focused on kinematics and slip distribution rather than slip magnitude.

The geometrical parameters used for these surfaces are summarized in Table 2-1. More detailed constraints for the geometry of the LOFS as well as the ChC and CCM are displayed in Figures 2-2 and 2-3, respectively. According to available evidence it was assumed that the LOFS cross-cuts the entire lithosphere, which implies that its depth is determined by the depth of the slab at each latitude, (~50 km in its northern end, ~6 km in its southern end).

Considerably fewer constrains are available with respect to the geometry of the ChC and the CCM. Both of these structures were modeled as discontinuities with strikes constrained by their surface-trace and with depths of 15 km according to estimations of the intra-arc seismogenic limit depth (*i.e.* brittle-plastic transition). The CCM is assumed to dip very steeply (85°) which is consistent with the geometry of numerous sub-

vertical/vertical feeder dikes (>100) and surface faults mapped at the Callaqui Strato-volcano [*Sielfeld et al*., 2016], that follow the overall ~N60°E fissure-like structure.

Table 2-1. Geometrical parameters considered to model the fault surfaces.

Faultsurface	Strike	Dip	Extension	Depth
LOFS-East	**N10**°E	**80**°W	**1100 km**	**10-50 km**
LOFS-West	**N10**°E	**70**°E	**600 km**	**10-50 km**
ChC	**N40°-70**°W	**60**°S	**180 km**	**15 km**
CCM	**N60**°E	**85**°N	**90 km**	**15 km**

2.5. Results

2.5.1 Interseismic model

Kinematics and fault slip rates calculated for the case studies during the interseismic phase of the SSC are shown in Figure 2-7. The Eastern master trace of the LOFS (Figure 7.a) displays pure strike-slip, dextral kinematics at a rate of 3.5 mm/yr in the south decreasing to 0.5 mm/yr in its northern termination. The Western master fault of the LOFS (Figure 7.b) displays reverse-dextral kinematics, with slip rates varying across the fault from 3.5 mm/yr along the southern portion, where dextral shear is localized, to 7 mm/yr of thrusting in the north. Results of right-lateral kinematics are consistent with the geological and seismic data from shallow focal mechanisms shown in Figure 3. Thrust behavior of the Western trace of the LOFS was observed by [*Lara et al*., 2008] and [*Thomson*, 2002]. Our results are consistent with these observations which suggest that this fault corresponds to the orogenic front at this latitude.

Figure 2-7.e, d displays interseismic kinematics and slip rates calculated for the NW-striking Chillán-Cortaderas (ChC) and for the ENE-striking Callaqui-Copahue-Mandolegue (CCM) faults, respectively. The ChC shows reverse-sinistral kinematics

with a minimum slip rate of 0.4 mm/yr in its eastern portion and a maximum of 1.4 mm/yr localized in its western termination. The rake of slip also increases to the west, with predominant thrusting where this structure changes its strike from N60°W to N40°W, right below the Nevados de Chillán volcanic complex. The CCM shows purely strike-slip dextral kinematics all across the fault at a maximum rate of 0.85 mm/yr localized in its central and shallow areas.

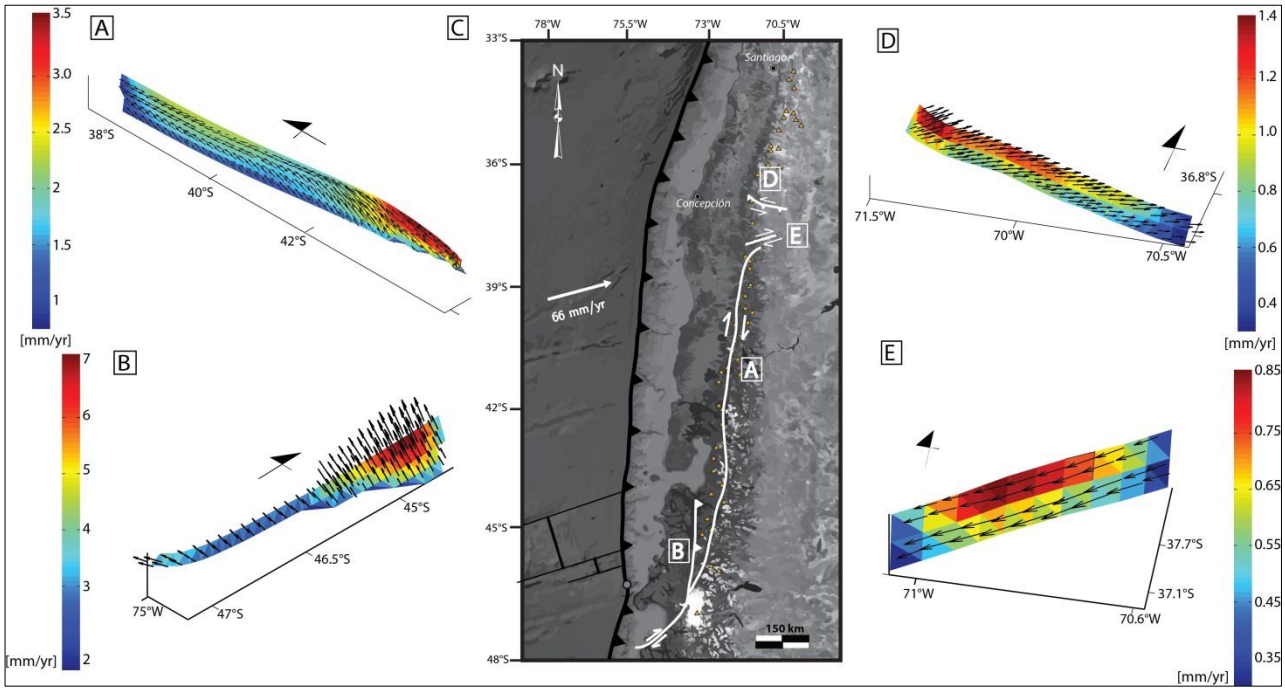

Figure 2-7. Results of Interseismic model. Kinematics and fault slip rate distribution with corresponding colorbar for: A) Eastern Master trace of the LOFS, B) Western Master trace of the LOFS, C) Regional map illustrating kinematics at case study faults D), E) Kinematics and fault slip rate distribution at Chillán-Cortaderas and E) Callaqui-Copahue-Mandolegue faults, respectively. North direction is shown for each case.

Because the boundary conditions on the case study faults were prescribed as zero normal displacement, normal traction magnitude and distribution on the faults due to interseismic loading can be computed (Figure 2-8). Elements on the LOFS (Figure 2-8.a, b) are subjected to compressive normal tractions (sign convention of tensile traction

positive was used). Compressive traction is also induced within the ChC (Figure 2-8.c), which displays maximum traction values of -4.5 kPa at its western area. The NE-striking CCM is subjected to tensile normal tractions of a maximum of 2kPa (Figure 2-8.d). This result is consistent with the presence of abundant dikes and of the fissure-like Callaqui volcano which follow the strike of this structure, confirming that ENE-striking faults are optimally oriented for tensile cracking during the interseismic period.

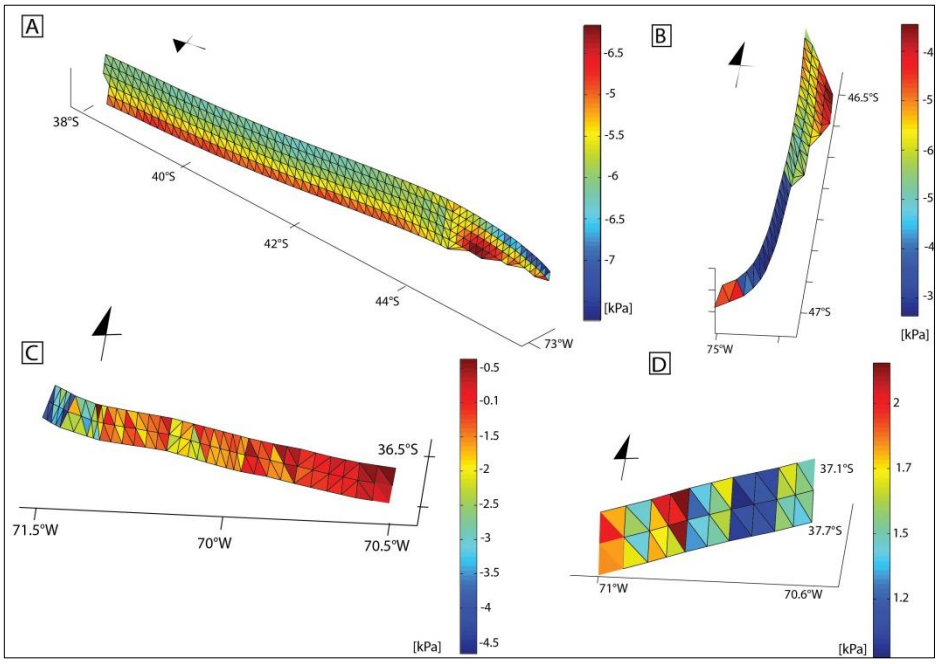

Figure 2-8. Normal traction distribution at case study faults during one year of loading during the interseismic period of the SSC (Tension positive). A) Eastern Master trace of the LOFS, B) Western Master trace of the LOFS, C) ChC and D) CCM faults.

2.5.2. Coseismic model

The deformation field resulting from the 2010 Maule earthquake induces a normal-sinistral behavior for the LOFS with the maximum slip localized at its northern end (Figure 2-9.a), which is the closest area of the fault to the rupture of the megathrust earthquake. The Western master trace of the LOFS (Figure 2-9.b) also displays normal kinematics due to this event but with a considerably lower slip as a result of the distance of this fault from the rupture area.

According to this model, during the coseismic phase induced by the Maule earthquake the ChC displays normal-dextral slip. The maximum slip is concentrated in the western portion of the surface, where the structure changes its strike to NNW which is also the exact surface location of the Nevados de Chillán volcanic complex, and decreases almost to 0 towards the east. The CCM also switches its kinematics during the coseismic phase induced by the Maule earthquake showing sinistral kinematics with maximum slip localized in its western-central and shallow area.

Normal traction distribution on the case study faults during the Maule event is shown in Figure 10. Tensile normal traction is induced at both master traces of the LOFS and within the western portion of the ChC, below the Nevados de Chillán volcanic complex, with a maximum traction of 0.6 MPa. On the contrary, the NE-striking CCM is exposed to compressional normal traction (negative values) as a result of the Maule rupture.

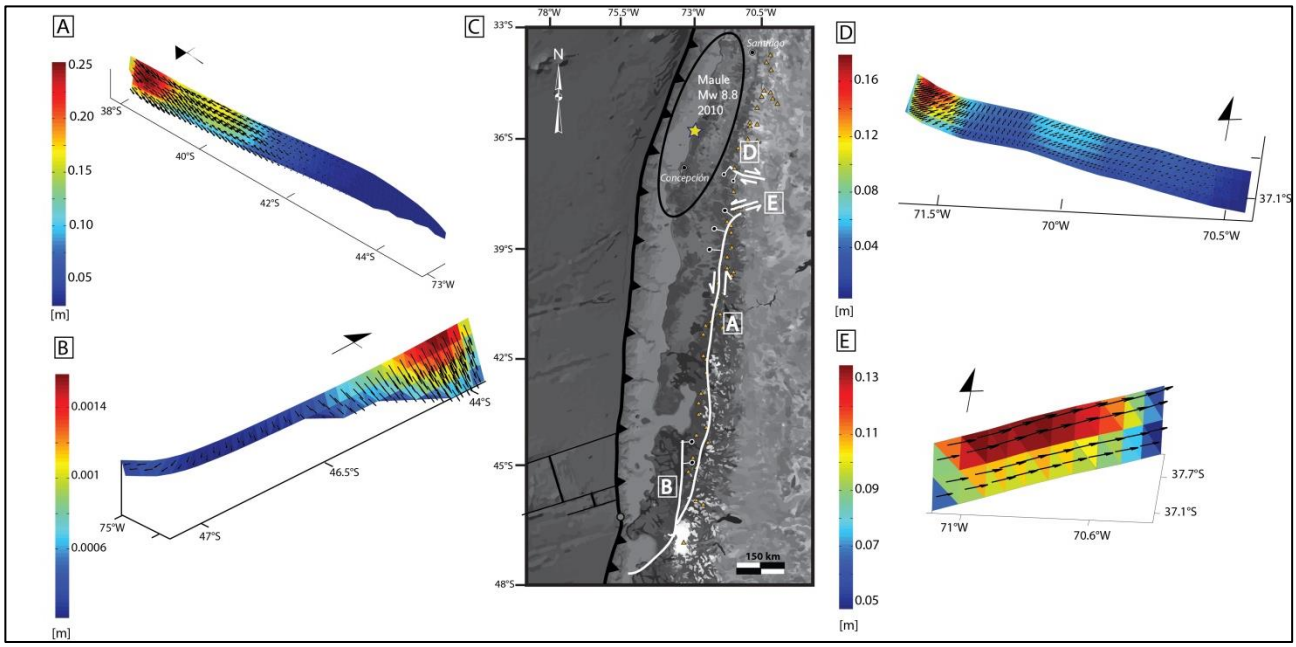

Figure 2-9. Results from Coseismic model. Kinematics and fault slip distribution with corresponding colorbar due to Maule earthquake for: A) Eastern Master trace of the LOFS, B) Western Master trace of the LOFS, D) ChC and E) CCM faults.

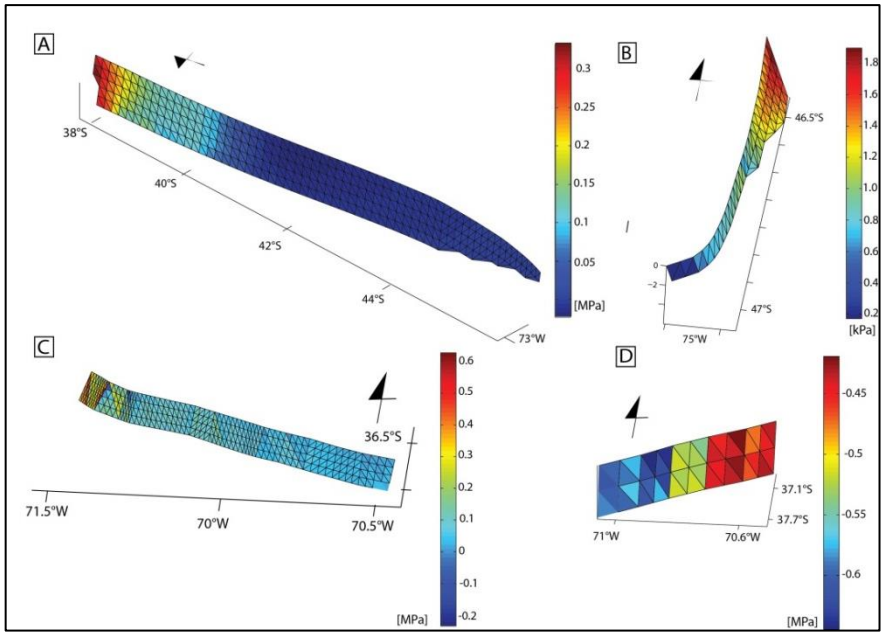

Figure 2-10. Normal traction distribution at case study faults due to Maule earthquake (Tension positive). A) Eastern Master trace of the LOFS, B) South-Western Master trace of the LOFS, C) ChC and D) CCM faults.

2.6. Discussion

2.6.1 Tectonic significance of margin-parallel and margin-transverse faults: A complex strain partitioning pattern

The convergence vector between the Nazca and South American plates is estimated to be 66 mm/yr [*Angermann et al.,* 1999] with a direction of N78°E [*Kendrick et al.,* 2003]. This results in an orthogonal-to-the-trench obliquity of ~22° where the Chilean margin trends N10°E (between 38°S and 47°S), and, further to the north, an obliquity of ~32° where the margin trends N20°E, (between 33°S and 38°S). This implies a trench-parallel component of convergence of 25 mm/yr for the former and of 35 mm/yr for the latter (Figure 2-11).

The magnitude of margin-parallel displacement that should be permanently accommodated within the upper crust should be calculated using the difference between the convergence angle and the direction of slip of interplate thrust earthquakes [*McCaffrey*, 1992; *Yu*, 1993]. According to this analysis, there are two extreme cases for strain partitioning within obliquely subducting margins: 1) Slip vectors of subduction zone earthquakes are orthogonal to the trench, in which case the partitioning is complete with all the margin-parallel component of oblique convergence being accommodated within the upper crust, and 2) Slip vectors of thrust earthquakes are parallel to the convergence vector, which implies a non-partitioned setting, with all the margin-parallel component of deformation being accommodated and released during thrust earthquakes.

We calculated representative slip vectors for 10 subduction thrust earthquakes in the SVZ (Table 2-2). Azimuth and plunge of the slip vectors are assumed to be the pole of the auxiliary nodal planes from the centroid moment tensor solutions [*Mccaffrey*, 1991]. We obtained a prevalent slip direction of N89°E which results in a slip vector residual of 13.5 mm/yr of margin-parallel displacement to be permanently accommodated in the

upper plate within 33°S and 38°S and of 13 mm/yr between 38°S and 47°S (Figure 2-11).

Table 2-2. Slip vectors of thrust earthquakes at the Southern Andes calculated as the pole of the auxiliary plane. (Global CMT catalog).

		Location			Fault Plane		Auxiliary Plane		Slip Vector	
Date	Mw	Lat	Long	Depth	Strike	Dip	Strike	Dip	Azimuth	Plunge
27-02-2010	8.8	-35,76	-72,473	30	14	19	179	71	89	19
16-03-2010	6.7	-36.124	-73.147	18	15	17	171	75	81	15
05-03-2010	6.6	-36.513	-73.116	35	4	21	184	69	94	21
14-07-2010	6.5	-38	-73.282	28	6	17	177	73	87	17
02-01-2011	7.1	-38.354	-73.275	25	2	15	179	75	89	16
11-02-2011	6.8	-36.344	-72.959	18	11	15	181	75	91	15
14-02-2011	6.6	-35.433	-72.739	25	16	21	190	70	100	20
25-03-2012	7.1	-35.183	-71.792	35	21	11	176	80	86	10
23-08-2014	6.25	-32.695	-71.442	32	19	29	183	62	93	28
20-06-2015	6.4	-36	-74	11	348	15	190	76	100	14

The amount of trench-parallel displacement accommodated by the LOFS in the Southern Andes has been evaluated in previous works [*Adriasola et al.*, 2006; *Rosenau et al.*, 2006; *Wang et al.*, 2007]. [*Rosenau et al.*, 2006], using a kinematic model, estimated a slip rate along the LOFS of 32 ± 6 mm/yr south of 40°S and 13 ± 3 mm/yr north from 40°S. These results are, however, strongly dependent on the width of the shear zone that is considered to be accommodating slip. [*Rosenau et al.*, 2006] assumed a shear zone width of 80 km in the north and of 150 km in the south; although no conclusive evidence of quaternary deformation encompassing this entire region has been found [*Lara et al.*, 2008]. In fact, recent paleo magnetic data from Southern Chile (38°S-41°S) documents in-situ rotation of blocks due to shear zone deformation is present within a 30 km wide sector adjacent to the LOFS [*Hernández-Moreno et al.*, 2016]. More conservative slip rates for the LOFS can be obtained from the observation of dextral offset of Miocene

plutons at the Reloncaví Fjord [*Adriasola et al.*, 2006; *Lara et al.*, 2008] which results in ~2.6 mm/yr of dextral slip rate along the LOFS since the Late Miocene. A short-term GPS-based maximum slip rate of 6.5 mm/yr is calculated for the fore-arc sliver west of the LOFS [*Wang et al*., 2007].

Results provided by our interseismic model show that the amount of margin-parallel deformation accommodated by the LOFS is of 3.5 mm/yr in the south decreasing to 0.5 mm/yr in its northern termination. These results imply that the LOFS is accounting for only ~30% of the residual margin parallel deformation at its Southern end. We have shown that the remainders of this deformation, which is particularly significant at the northern termination of the LOFS, has to be accommodated elsewhere, either within the fore-arc and/or by other crustal faults, not necessarily margin-parallel, as has been commonly assumed. To further assess the implications of our findings, we modeled NW-striking (ChC) and ENE-striking (CCM) crustal discontinuities in an attempt to represent the numerous transverse faults existing along the Andean arc. We found that NW-striking faults can accommodate a maximum of 0.9 mm/yr of strike-slip deformation by sinistral kinematics and 1 mm/yr of thrusting whereas ENE-striking faults behave as purely dextral with the potential of accommodating 0.85 mm/yr of strike-slip deformation. This shows that transverse faults are capable of absorbing a significant amount of plate-boundary deformation arising from oblique convergence.

The difference between the slip rate for the LOFS calculated here and the GPS derived slip rate by Wang et al. (2007) may be a consequence of the subduction of the Chile Rise at the Chile Triple Junction. It has been suggested that this process is contributing considerably to the northward motion of the fore-arc sliver located west of the fault [*e.g. Forysthe and Nelson*, 1985; *Thomson* 2002]. This variable was not considered in our model because we attempted to calculate the amount of deformation that can be accommodated at crustal faults only due to oblique subduction; therefore our model, which produces the maximum possible slip rate on the LOFS driven solely by subduction obliquity, may underestimate the actual LOFS slip rate.

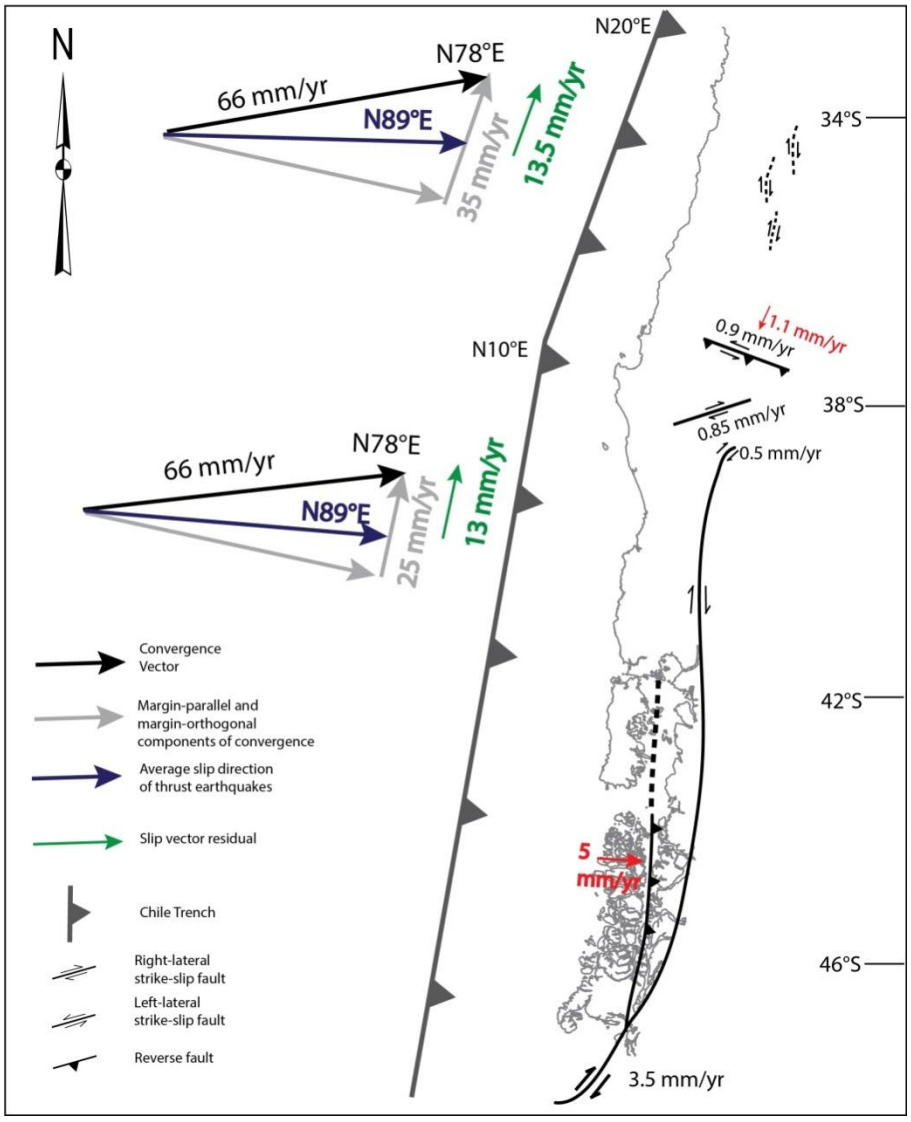

Figure 2-11. Schematic illustration showing strain partitioning due to oblique subduction at the Southern Andes. Between 33°S and 38°S, the trench trends N20°E which results in a total of 35 mm/yr of margin-parallel deformation. Blue arrow shows the direction of slip of megathrust earthquakes at the area, because this vector is not orthogonal to the trench, some part of the margin-parallel deformation is released during thrust events. The same is shown for the Southern Andes between 38°S and 47°S where the trench trends N10°E. To the right, approximate location of the faults selected as case studies with their interseismic kinematics and estimated slip rates. Black and red arrows indicate strike-slip and dip-slip rates, respectively.

2.6.2 Coseismic deformation at intra-arc faults

According to our coseismic simulations, crustal faults have the potential to switch their kinematics during (or soon after) megathrust events. Geological evidence of this duality in kinematic behavior of faults was found in an intra-arc NW-striking fault by [*Pérez-Flores et al.*, 2016] who demonstrated the presence of two governing stress regimes as a result of dynamic analysis of fault slip data. The first and more predominant stress regime is consistent with sinistral-reverse kinematics of the fault whereas the second accounts for normal kinematics. Similar results are found by [*Vargas et al.*, 2013] at the LOFS: they report evidence of occasional fault slip data registering extensional behavior at outcrops associated with the southern portion of the LOFS (Aysen Fjord), which appear to be inconsistent with the predominance of right lateral- reverse kinematics for this fault system.

Furthermore, NW-striking faults within the Andes exhibit extensional behavior temporally controlled by the coseismic period of the SSC. This was the case for the NW-striking Pichilemu Fault in the fore-arc, which displayed crustal earthquakes of maximum Mw 7.0, with normal kinematics, eleven days after the Maule event [*Farías et al.*, 2011; *Aron et al.*, 2013, 2014]. Field evidence at this and other NW-striking fore-arc faults suggests that extensional kinematics controls the overall architecture of the fore-arc, meaning that the coseismic phase of the SSC governs the structural grain at these domains. At the intra-arc though, this relationship is not clear. Evidence of increased volcano-tectonic activity has been reported during the coseismic phase of the SSC at volcanic complexes emplaced on top of NW-striking basement faults [*Sepúlveda et al.*, 2005; *Bonali*, 2013]. At Nevados de Chillán volcanic complex [*Farías et al.*, 2014] found increased volcano-tectonic activity after an aftershock of the Maule event, which they associate with dilatation-induced fluid migration within the complex.

Our results also shed light on spatio-temporal clamping/unclamping of magma pathways throughout the SVZ during the SSC. We obtain long-term sinistral-reverse kinematics for the NW-striking ChC during the interseismic phase of the SSC, with compressive normal tractions induced on the fault (Figure 8.c) which makes magma transport to feed the volcanic complex emplaced on top of it unlikely. During the coseismic displacement field induced by the Maule earthquake, the ChC displays normal kinematics, with maximum tensile normal tractions of 0.6 MPa concentrated right below the location of Nevados de Chillan volcanic complex. In addition, the northern portion of the LOFS, closest to the Maule rupture, exhibits normal kinematics due to the Maule earthquake. On the contrary, NE-striking faults are subjected to tensile tractions during the interseismic period of the SSC (Fig. 8.d), facilitating magma ascent on the long-term time scale, which is consistent with field evidence by *Pérez-Flores et al.*, 2016.

Because of the long time lapse encompassing an interseismic phase of the SSC in the area (at least 175 years for the Maule segment, *Vigny et al*., 2011) and the relatively low coseismic slip induced on the faults with respect to accumulated interseismic slip, we propose that secular kinematics should prevail in the structural grain of intra-arc faults; however, we showed that the elastic rebound produced during the coseismic phase induces non-negligible extensional behavior at intra-arc faults, particularly at NW-striking and margin-parallel faults. As a result NW structures, which as we showed are misoriented with respect to the interseismic stress field to promote magma ascent, can become pathways for seismically pumped magmas, as proposed by [*Lara et al.*, 2004]. The same could occur for margin-parallel faults, which during the interseismic are dominated by a transpressive stress regime making unlikely a quasi-instantaneous ascent of primitive magma necessary to explain the presence of monogenic cones with tholeiitic signature emplaced on the trace of the LOFS, thus these cones might be the result of megathrust earthquake extension triggering at the LOFS.

2.6.3 Maximum earthquake estimation for modeled faults

The maximum expected earthquakes on faults selected as case studies can be estimated by the use of the interseismic slip rates calculated in the numerical model. Considering the approach by [*Hanks and Kanamori,* 1979] it is possible to calculate the geometric momentM_0, and the seismic momentM_w, as shown in equations 2 and 3

$$M_0 = L(m)W(m)s\left(\frac{m}{yr}\right)\mu(Pa) \quad Equation\ 2-2$$

$$M_w = \frac{2}{3} * log_{10}(M_0 * T) - 9.1 \quad Equation\ 2-3$$

where L and W represent the length and width of the rupture respectively, $s$accounts for the maximum slip rate along the fault and μ is the shear modulus, assumed equal to $30GPa$for the continental crust. T is the recurrence interval in years for a crustal earthquake at each fault. Because this is an unknown variable, we prescribed values of T of 100 and 1000 years representing illustrative lower and upper bounds, respectively. The geometrical parameters used in this analysis are those displayed in Table 1. For the ChC L is restricted to the length of the fault that according to the model's results is more likely to slip (~20 km long). With respect to the LOFS, to consider a complete rupture would be an extremely unlikely scenario. We considered fault lengths of the main branches of the fault mapped by [*Vargas et al.,* 2013], who obtained maximum lengths of 15-20 km at the Aysen Fjord. The magnitudes of M_w calculated for the each of the case studies considering different recurrence intervals are shown in table 3.

Table3. Maximum earthquake estimations at modeled faults.

Parameter	LOFS	ChC	CCM
$\mathbf{M_0}$ (N-m)	$3.15 * 10^{16}$	$1.26 * 10^{16}$	$1.78 * 10^{16}$
$\mathbf{M_w\ T = 100\ yrs}$	6.27	6.00	6.1
$\mathbf{M_w\ T = 1000\ yrs}$	6.93	6.66	6.77

2.6.4 Model significance and limitations

To implement the numerical model of crustal deformation within the Chilean Margin presented here, we made a number of assumptions in idealizing the problem. Poly3d simulates the mechanical interaction of geometrically complex discontinuities in a homogeneous and isotropic elastic half space of small deformations. Here we examine the potential impact of these assumptions.

First, elastic constitutive behavior cannot capture all of the complexity of the lithospheric response during the SSC: in reality, a certain amount of viscoelastic relaxation occurs months to years after a megathrust earthquake (*i.e.*, the post-seismic phase of the SSC). It has been shown, however, that crustal deformation due to the elastic interplay during the interseismic and coseismic phases of the SSC can be approximated quite accurately using dislocation-based elastic models [*Dragert et al.*, 1994; *Klotz et al.*, 2006] actual interseismic stress fields may –however-be influenced by the viscoelastic deformation years after a megathrust earthquake [*Wang et al.*, 2007]. This post-seismic perturbation is constrained locally to the rupture area of the earthquake and temporally to tens of years of influence [*Hu et al.*, 2004]. Because our approach is intended to represent the interseismic stress field throughout multiple subduction seismic cycles, post-seismic deformation can be considered as local and temporal anomalies that should not prevail in the long-term structural grain of the upper crust.

Second, the modeling technique used here considers a semi-infinite, faulted, but otherwise isotropic medium. Because we are interested in the deformation of the upper crust, we used elasticity constants representing the average continental crust elastic properties. The assumption of isotropy is very reasonable at the southern portion of the model (38°S-47°S) where the crust is composed almost entirely of a granitic batholith (Patagonian Batholith); however, the northern portion (33°S-38°S) is covered by a thick volcano-sedimentary layer that induces variability in the elastic response of the medium.

Recent work incorporating rock anisotropy into BEM solutions has shown that such anisotropy can lead to significant differences in the predicted surface displacement fields near faults [*e.g. Pan et al.*, 2014]. At the large scale of our simulations, however, we expect that this assumption contributes some error to our computed displacement fields, but the first order patterns should hold.

The assumption of the subduction process being quasi-static implies that surface deformation rates remain constant throughout the interseismic period [*Klotz et al.*, 2006]. Due to the time-scale period that encompasses a single subduction seismic cycle, which is at least 175 years for the Maule area [*Vigny et al.*, 2011], and the very recent development of GPS technologies, there is very limited information regarding time-dependent processes for locking distribution and therefore time-dependent surface deformation variability during the interseismic period. Thus, in order to understand the deformation pattern through multiple seismic cycles, assuming constant deformation rates is a reasonable consideration.

The use of elastic and quasi-static modeling techniques also raises the question of what is the significance of the model results in terms of long-term deformation patterns. A certain amount of the deformation induced by the subduction of the Nazca Plate is not released during thrust earthquakes, but is permanently accommodated in the upper crust in crustal faults and in the thickening of the crust. Rough estimations predict that 10% of the interseismic deformation is not released in earthquakes but is permanently accommodated within the overriding plate [*Jordan et al.*, 1993]. This permanent deformation is responsible for shaping the long-term structural grain of the upper crust and thus for building the orogenic belt.

We contrasted our model results with GPS-derived velocities, which represent the quasi-instantaneous strain field within the upper crust. [*Allmendinger et al.*, 2005] showed for the central Andes that there is a surprisingly good correlation between geologic

observation of long-term deformation patterns and GPS, thus quasi-instantaneous, deformation. They interpret that some of the interseismic deformation field must reflect permanent deformation, which implies that the elastic and permanent deformation patterns are similar because both of them are a result of the same stress field. Consequently, the good fit between calculated surface deformation vectors and GPS-derived vectors allows considering our results as estimations of the deformation in the upper crust due to oblique subduction in the long-term time-scales, whereas areas of poor fit indicate regions of geologic complexity not currently captured in the models. These results imply that our model implementation constitutes a new methodology that can be furtherly used to simulate the elastic response of crustal faults within any region of the Andes to interseismic and coseismic loading. This can help constrain kinematics, slip rates and asses seismic hazard on crustal faults with very limited data

2.7 Conclusions

1) The interseismic deformation regime due to oblique subduction can be modeled using a forward BEM approach. Surface deformation calculated by this modeling technique is contrasted with GPS derived deformation vectors, obtaining an overall fit of 1-40%, which suggests that this method is suitable to simulate the long-term deformation field in the overriding plate. The coseismic deformation induced by a megathrust earthquake can be modeled by prescribing previously calculated slip distributions at the plate's interface.
2) The margin-parallel LOFS displays dextral-reverse kinematics during the interseismic period of the subduction seismic cycle, its South-Western master Fault accommodates mostly shortening at a maximum rate of 5 mm/yr whereas the eastern master Fault displays strike-slip, dextral kinematics at a maximum rate of 3.5 mm/yr.

3) NW-striking transverse faults represented here by the ChC, display sinistral-reverse kinematics during the interseismic phase of the SSC, with the potential of accommodating a maximum slip of 1.4 mm/yr. ENE-striking faults display strike-slip dextral kinematics, with a maximum slip of 0.85 mm/yr.
4) The total amount of margin-parallel displacement that should be permanently accommodated in the upper crust in the Southern Andes is of 13.5 mm/yr where the margin strikes N20°E (33°S-38°S) and of 13 mm/yr where the margin strikes N10°E (38°S-47°S), which was calculated considering the angle of deviation between the convergence vector and the direction of slip of megathrust earthquakes. The LOFS accounts for ~30% of this deformation at its Southern end; the remaining is accommodated at margin-transverse faults which results in a complex strain partitioning pattern.
5) During the coseismic deformation regime induced by the Maule 2010 earthquake the modeled faults switch their kinematics: NE-striking fault become sinistral while NW-striking faults behave as normal-dextral. We propose that in the long-term, the strike-slip behavior of these faults will be controlled by their interseismic kinematics. However, at NW-striking faults the coseismic extension is significant, which if combined with a close to lithostatic fluid pressure, it is very likely that these faults can account for seismic cycle-controlled magma pathways for the volcanic complexes emplaced on top of them and express dual kinematic behavior, which is consistent with field evidence.
6) Maximum moment magnitudes in the range of Mw 6 to 6.67 can be expected for crustal earthquakes with the ChC geometry considered here, whereas a maximum of Mw 6.1 to 6.77 earthquakes could occur in the CCM. Considering fault lengths mapped by previous authors at the LOFS, crustal earthquakesare expected to reach up to Mw 6.9.

REFERENCES

Acocella, V., and F. Funiciello (2009), Kinematic setting and structural control of arc volcanism, Earth Planet. Sci. Lett., doi:10.1016/j.epsl.2009.10.027.

Acocella, V., Gioncada, A., Omarini, R., Riller, U., Mazzuoli, R., & Vezzoli, L. (2011). Tectonomagmatic characteristics of the back-arc portion of the Calama–Olacapato–El Toro Fault Zone, Central Andes. Tectonics, 30(3), TC3005. doi:10.1029/2010TC002854

Adriasola, A. C., S. N. Thomson, M. R. Brix, F. Hervé, and B. Stockhert (2006), Postmagmatic cooling and late Cenozoic denudation of the North Patagonian Batholith in the Los Lagos region of Chile, 41°-42° 15'S, *Int. J. Earth Sci.*, *95*(3), 504–528, doi:10.1007/s00531-005-0027-9.

Allmendinger, R. W., R. Smalley, M. Bevis, H. Caprio, and B. Brooks (2005), Bending the Bolivian orocline in real time, *Geology*, *33*(11), 905–908, doi:10.1130/G21779.1.

Allmendinger, R. W., Ramos, V. A., Jordan, T. E., Palma, M. & Isacks, B. L. (1983). Paleogeography and Andean structural geometry, northwest Argentina. Tectonics, 2, 1–16.

Anderson, E.M., (1951). The Dynamics of fauting. Edingburgh: Oliver and Boyd.

Angermann, D., J. Klotz, and C. Reigber (1999), Space-geodetic estimation of the Nazca-South America Euler vector, *Earth Planet. Sci. Lett.*, *171*(3), 329–334, doi:10.1016/S0012-821X(99)00173-9.

Aron, F., R. W. Allmendinger, J. Cembrano, G. González, and G. Yáñez (2013), Permanent fore-arc extension and seismic segmentation : Insights from the 2010 Maule earthquake , Chile, , *118*(1), 724–739, doi:10.1029/2012JB009339.

Aron, F., J. Cembrano, F. Astudillo, R. W. Allmendinger, and G. Arancibia (2014), Constructing forearc architecture over megathrust seismic cycles: Geological snapshots from the Maule earthquake region, Chile, *Geol. Soc. Am. Bull.*, *127*(3-4), 464–479, doi:10.1130/B31125.1.

Beck, M. E. (1991), Coastwise transport reconsidered: lateral displacements in oblique subduction zones, and tectonic consequences, *Phys. Earth Planet. Inter.*, *68*(1-2), 1–8, doi:10.1016/0031-9201(91)90002-Y.

Beck, M. E., C. Rojas, and J. Cembrano (1993), On the nature of buttressing in margin-parallel s-146trike-slip fault systems, *Geology*, *21*, 755–758.

Bevis, M., and S. J. Martel (2001), Oblique plate convergnce and interseismic strain accumulation, *Geochem. Geophys. Geosyst. (2)*, 200GC000125.

Bonali, F.L, Corazzato C., Tibaldi, A., (2011), Elastic stress interaction between faulting and volcanism in the Olacapatp-San Antonio de Los Cobres area (Puna plateau, Argentina), *Glob Planet Change 90-91*, 104-120.

Bonali, F. L. (2013), Tectonophysics Earthquake-induced static stress change on magma pathway in promoting the 2012 Copahue eruption, *Tectonophysics*, *608*, 127–137, doi:10.1016/j.tecto.2013.10.006.

Brown, M., Solar, G., (1998). Granite ascent and emplacement during contractional deformation in convergent orogens. *J. Struct. Geolog*. 20, 1365-1393.

Brogi, A., Liotta, D., Meccheri, M., Fabbrini, L., (2010), Transtensional shear zones controlling volcanic eruptions: the Middle Pleistocene Mt Amiata volcano (inner Northern Apennines, Italy). *Terra Nova*, 22 (2), 137-146.

Burgers, J., (1939) Internal strains in solids. *Proc. Acad. Sci*. 42, 293.

Cashman, S.M., Kelsey, H.M., Erdman, C.F., Cutten, H.N.C., Berryman, K. R., (1992), Strain partitioning between structural domains in the forearc of the Hikurangi subduction zone, New Zealand. *Tectonics, (11)*, 242-257.

Cembrano, J., Moreno, H., (1994), Geometría y naturaleza contrastante del volcanismo Cuaternario entre los 38° S y 46° S: ¿Dominios compresionales y tensionales en un régimen transcurrente? *Congreso Geológico Chileno, No. 7*, Actas, Vol. 1. Universidad de Concepción, Chile, pp. 240–244.

Cembrano, J., and L. Lara (2009), The link between volcanism and tectonics in the southern volcanic zone of the Chilean Andes: A review, *Tectonophysics*, *471*(1-2), 96–113, doi:10.1016/j.tecto.2009.02.038.

Cembrano, J., F. Hervé, and A. Lavenu (1996), The Liquiñe Ofqui fault zone: a long-lived intra-arc fault system in southern Chile, *Tectonophysics*, *259*(1-3), 55–66, doi:10.1016/0040-1951(95)00066-6.

Cembrano, J., E. Schermer, A. Lavenu, and A. Sanhueza (2000), Contrasting nature of deformation along an intra-arc shear zone, the Liquiñe–Ofqui fault zone, southern Chilean Andes, *Tectonophysics*, *319*(2), 129–149, doi:10.1016/S0040-1951(99)00321-2.

Chernicoff, C.J. (2001). Interpretación geofísico-geológica del levantamiento aeromagnético de la región noroccidental de la Provincia de Chubut. *Revista de la Asociación Geológica Argentina, 56(3)*, p. 268-280.

Chinn, D.S., Isacks B.L., (1983), Accurate source depths and focal mechanisms of shallow earthquakes in western South America and in the New Hebrides island arc. *Tectonics 2(6)*, 529-563.

Chinnery, M., (1963), The stress changes that accompany strike-slip faulting. *Bull. Seismol. Soc. Am.* 53, 921-932.

Comninou, M., Dundurs, J., (1975), The angular dislocation in a half space. *J. Elast.* 5 (3), 203-216.

Corazzato, C., Tibaldi, A., (2006), Fracture control on type, morphology and distribution of parasitic volcanic cones: an example from Mt. Etna, Italy. *J. Volc. Geotherm. Res*. 158, 177-194.

Crouch, S.L., (1976), Solution of plane elasticity problems by the displacement discontinuity method, *Int. J. Numer. Methods in Engineer.(10)*, 301-343.

Crouch, S.L., Starfield, A.M., (1983), Boundary element methods in solid mechanics: With applications in rock mechanics and geological engineering: London, Unwin Hyman, 322 p.

Dair, L., M. L. Cooke, (2009), San Andreas fault geometry through the San Gorgonio Pass , California, , 119–123, doi:10.1130/G25101A.1.

Dixon, H. J., Murphy, M. D., Sparks, S. J. (1999). The geology of Nevados de Chillán volcano,

Chile. *Revista Geológica de Chile, 26*, 227–253.

Dragert, H., R. Hyndman, C. Rogers, and K. Wang (1994), Current deformation and the with of the seismogenic zone of the northern Cascadia subduction thrust, *J. Geophys. Res.*, *99*(B1), 653–668.

Dziewonski, A., G. Ekström, Woodhouse, J.H., Zwart, G., (1990), Centroid-moment tensor solutions for January — March 1989, *Phys. Earth Planet. Inter.*, *59*(4), 233-242.

Dziewonski, A., G. Ekström, Maternovskaya, N.N (2000), Centroid-moment tensor solutions for January — March 1989, *Phys. Earth Planet. Inter.*, *118*, 21-11.

Farias, M., D. Comte, and R. Charrier (2006), Sismicidad superficial en Chile central: Implicancias para el estado cortical y crecimiento de los Andes Centrales australes, *XI Congr. Geol. Chil.*, *1*(1), 403–406.

Farías, M., D. Comte, S. Roecker, D. Carrizo, and M. Pardo (2011), Crustal extensional faulting triggered by the 2010 Chilean earthquake : The Pichilemu Seismic Sequence, , *30*(November), 1–11, doi:10.1029/2011TC002888.

Farías, C., Lupi, M., Fuchs, F., Miller, S., (2014), Seismic activity of the Nevados de Chillán volcanic complex after the 2010 Mw8.8 Maule, Chile, earthquake, *J. Volc. Geoth. R.*, doi:10.1016/j.jvolgeores,2014.06.2013.

Fitch, T. (1972), Plate Convergence, transcurrent faults, and internal deformation adjacent to southeast Asia and the western Pacific, *J.Geophys. Res., 77(23)*, 4432-4460, doi:10.1029/JB077i023p04432.

Folguera, A., Ramos, V.A., Hermanns, R.L., Naranjo, J., (2004). Neotectonics in the foothills of the southernmost central Andes (37°-38°S): evidence of strike-slip displacement along the Antiñir-Copahue fault zone, *Tectonics 23 (5)*, 541-566.

Forysthe, R., and E. Nelson (1985), Geological manifestations of ridge collision: Evidence from the Golfo de Penas-Taitao basin, southern Chile, *Tectonics*, *4(5)*, 477-495, doi:10.1029/TC004i005p00477.

Glodny, J., H. Echtler, S. Collao, M. Ardiles, P. Burn, and O. Figueroa (2008), Differential Late Paleozoic active margin evolution in South-Central Chile (37° S-40°S) - the Lanalhue Fault Zone, *J. South Am. Earth Sci.*, *26*(4), 397–411, doi:10.1016/j.jsames.2008.06.001.

Guinebertau, B., Bouchez, J., Vigneresse, J.,(1987). The Mortagne granite pluton (France) emplaced by pull-apart along a shear zone: structural and gravimetric arguments and regional implication. *Geolog. Soc. Am.*, Bulletin 99, 763-770.

Griffith, W. A., and M. L. Cooke (2004), Mechanical Validation of the Three-Dimensional Intersection Geometry between the Puente Hills Blind-Thrust System and the Whittier Fault , Los Angeles , California, , *94*(2), 493–505.

Griffith, W. A., and M. L. Cooke (2005), How Sensitive Are Fault-Slip Rates in the Los Angeles Basin to Tectonic Boundary Conditions ?, , *95*(4), 1263–1275, doi:10.1785/0120040079.

Haberland, C., A. Rietbrock, D. Lange, K. Bataille, and S. Hofmann (2006), Interaction between

forearc and oceanic plate at the south-central Chilean margin as seen in local seismic data, , *33*(June 2005), 1–5, doi:10.1029/2006GL028189.

Hanks, T.C., Kanamori, H., (1979), A moment magnitude scale, *J. Geophys. Res. (84)*, 2348-2350.

Hayes, G. P., D. J. Wald, and R. L. Johnson (2012), Slab1 . 0 : A threedimensional model of global subduction zone geometries, *117*(January), 1–15, doi:10.1029/2011JB008524.

Hernandez-Moreno, C., F. Speranza, and A. Di Chiara (2014), Understanding kinematics of intra-arc transcurrent deformation: Paleomagnetic evidence from the Liquiñe-Ofqui fault zone (Chile, 38–41° S), *Tectonics, 33(10),* 1964–1988, doi:10.1002/2014TC003622.

Hernandez-Moreno, C., F. Speranza, and A. Di Chiara (2016), Paleomagnetic rotation pattern of the shouthern Chile fore-arc sliver (38°S-42°S): A new tool to evaluate plate locking along subduction zones, *J. Geophys. Res. Solid Earth, 121,* doi:10.1002/2015JB012382.

Hervé, F. (1976), Estudio Geológico de la falla Liquiñe-Reloncaví en el área de Liquiñe; Antecedentes de un movimiento transcurrente (Provincia de Valdivia), *Acta. Congr, Geol. Chil, 1,* B39-B56.

Hervé, F. (1994), The Southern Andes between 39°S and 44°S latitude: The geological signature of transpressive tectonic regime related to a magmatic arc, in *Tectonics of the Southern Central Andes*, pp. 243-248, Springer, Berlin.

Hoffmann-Rothe, A., N. Kukowski, G. Dresen, H. Echtler, O. Oncken, J. Klotz, E. Scheuber, and A. Kellner (2006), Oblique Convergence along the Chilean Margin: Partitioning, Margin-Parallel Faulting and Force Interaction at the Plate Interface, *The Andes*, 125–146, doi:10.1007/978-3-540-48684-8_6.

Holford,S., R. Hillis, M. Hand, M. Sandiford, (2011), Thermal weakening localizes intraplate deformation along the southern Australian continental margin, *Earth and Planetary Science Letters*, 305: 207-214, doi. /10.1016/j.epsl.2011.02.056.

Hu, Y., K. Wang, J. He, J. Klotz, and G. Khazaradze (2004), Three-dimensional viscoelastic finite element model for postseismic deformation of the great 1960 Chile earthquake, *J. Geophys. Res. B Solid Earth*, *109*(12), 1–14, doi:10.1029/2004JB003163.

Hutton, D.H.W., (1982). A tectonic model for the emplacement og the Main Donegal Granite, NW Ireland.*J. Geolog. Soc. of London* 139, 615-631.

Hutton, D.H.W., (1988). Granite emplacement mechanism and tectonic controls: inferences from defromation studies. *Trans. of the Roy. Soc. of Edinburgh, Earth Science* 79, 245-255.

Islam R., (2009), Origin of the regional stress field along the Liquiñe-Ofqui Fault Zone (LOFZ), Southern Chilean Andes by means of FE simulations, J. Mt. Sci. (6), 1-13, doi:10.1007/s11629-009-0253-X.

Iturrieta, P., Hurtado D., Cembrano J., Valderrama C., Stanton-Yonge A., (2015), Finite Element Stress Model of a Strike-Slip Duplex: A case study from Southern Chile, AGU Fall Meeting, Am. Geophys. Un., San Francisco, CA.

Jackson, J., (1992), Paritioning of strike-slip and convergent morion between Eurasia and Arabia in Eastern Turkey and the Caucasus, *J. geophys. Res. (97)*, 12471-12479.

Jarrard, R. D. (1986a), Relations among subduction parameters, *Rev. Geophys.*, *24*(2), 217–284, doi:10.1029/RG024i002p00217.

Jarrard, R. D. (1986b), Terrane motion by strike-slip faulting of forearc slivers, , (September), 780–783.

Jordan, T.E., Isacks, B.L., Allmendinger, R.W., Brewer, J.A., Ramos, V.A., Ando, C.J., (1983). Andean tectonics related to geometry of subducted Nazca plate. GSA Bulletin 94, 341–361.

Jordan T., Isacks B, Ramos VA, Allmendinger RW., (1983b) . Mountain building model: The Central Andes. *Episodes* 1983 (3):20-26.

Jordan, T. E., R. W. Allmendinger, J. F. Damanti, and R. E. Drake (1993), Chronology of Motion in a Complete Thrust Belt: The Precordillera, 30-31°S, Andes Mountains, *J. Geol.*, *101*(2), 135–156, doi:10.1086/648213.

Katz, H.R. (1971), Continental margin in Chile; is tectonic style compressional or extensional? *Am. Assoc. of Petr. Geol.*, 55(10), p. 1753-1758.

Kendrick, E., M. Bevis, R. Smalley, B. Brooks, R. B. Vargas, E. Lauría, and L. P. S. Fortes (2003), The Nazca-South America Euler vector and its rate of change, *J. South Am. Earth Sci.*, *16*(2), 125–131, doi:10.1016/S0895-9811(03)00028-2.

Klotz, J., A. Abolghasem, G. Khazaradze, B. Heinze, T. Vietor, R. Hackney, K. Bataille, R. Maturana, J. Viramonte, and R. Perdomo (2006), Long-Term Signals in the Present-Day Deformation Field of the Central and Southern Andes and Constraints on the Viscosity of the Earth's Upper Mantle, *Andes SE - 4*, 65–89, doi:10.1007/978-3-540-48684-8_4.

Lange, D., J. Cembrano, A. Rietbrock, C. Haberland, T. Dahm, and K. Bataille (2008), First seismic record for intra-arc strike-slip tectonics along the Liquiñe-Ofqui fault zone at the obliquely convergent plate margin of the Southern Andes, *Tectonophysics , 455(1-4)*, 14-24, doi:10.1016/j.tecto.2008.04.014.

Lara, L. E., J.A. Naranjo, H. Moreno (2004), Rhyodacitic fissure eruption in Southern Andes (Cordón Caulle; 40.5°S) after the 1960 (Mw:9.5) Chilean earthquake: a structural interpretation, *J. Volcanol. Geotherm. Res. (138)*, 127-138, doi:10.1016/j.jvolgeores.2004.06.009.

Lara, L. E., A. Lavenu, J. Cembrano, and C. Rodríguez (2006), Structural controls of volcanism in transversal chains: Resheared faults and neotectonics in the Cordón Caulle-Puyehue area (40.5°S), Southern Andes, *J. Volcanol. Geotherm. Res.*, *158*(1-2), 70–86, doi:10.1016/j.jvolgeores.2006.04.017.

Lara, L.E., Cembrano, J., Lavenu, A., (2008), Quaternary vertical displacement along the Liquiñe-Ofqui Fault Zone: Differential Uplift and coeval volcanism in the Southern Andes?, *Int. Geol. Rev. (50)*, 1-19, doi: 10.2747/0020-6814.50.4.1.

Lavenu, a, and J. Cembrano (1999), Compressional and transpressional stress pattern for the Pliocene and Quaternary (Andes of central and southern Chile), *J. Struct. Geol.*, *21*, 1669–1691, doi:10.1016/S0191-8141(99)00111-X.

Legrand, D., Barrientos, S., Bataille, K., Cembrano, J., Pavez, A., (2011), The fluid-driven tectonic swarm of Aysen Fjord, Chile (2007) associated with two earthquakes (Mw =6.1 and Mw=6.2) within the Liquiñe-Ofqui Fault Zone, *Continent. Shelf Res.*, 31, 154-161,

doi:10.1016/j.csr.2010.05.008.

Lin, Y. N. et al. (2013), Coseismic and postseismic slip associated with the 2010 Maule Earthquake, Chile: Characterizing the Arauco Peninsula barrier effect, *J. Geophys. Res. Solid Earth*, *118*(6), 3142–3159, doi:10.1002/jgrb.50207.

López-Escobar, L., Cembrano, J., Moreno, H. (1995), Geochemistry and tectonics of the Chilean Southern Andes basaltic Quaternary Volcanism (37°-46°S). *Revista Geológica de Chile*,*(22*), No. 2 pp.219-234.

Maerten, F., L. Maerten, and D. D. Pollard (2014), Computers & Geosciences iBem3D , a three-dimensional iterative boundary element method using angular dislocations for modeling geologic structures, *Comput. Geosci.*, *72*, 1–17, doi:10.1016/j.cageo.2014.06.007.

Maerten, L., P. Gillespie, and D. D. Pollard (2002), Effects of local stress perturbation on secondary fault development, , *24*, 145–153.

Marone, C., Scholz C., Bilham, R., (1991), On the Mechanics of Earthquake Afterslip, *J. Geophys. Res. (96)*, p. 8441-8452.

Marshall, S. T., M. L. Cooke, and S. E. Owen (2008), Effects of Nonplanar Fault Topology and Mechanical Interaction on Fault-Slip Distributions in the Ventura Basin , California, , *98*(3), 1113–1127, doi:10.1785/0120070159.

Mccaffrey, R. (1991), Slip vectors and stretching of the Sumatran fore arc, *Geology (19)*, 881–884.

McCaffrey, R. (1992), Oblique plate convergence, slip vectors, and forearc deformation, J. Geophys. Res., 97(92), 8905-8915, doi:10.1029/92JB00483.

Melnick, D., and H. P. Echtler (2006), Morphotectonic and Geologic Digital Map Compilations of the South-Central Andes (36 °–42 ° S), in *The Andes - Active subduction Orogeny: Frontiers in Earth Sciences*, edited by O. Oncken et al., pp. 565-568, Springer, Berlin.

Melnick, D., A. Folguera, and V. A. Ramos (2006), Structural control on arc volcanism: The Caviahue–Copahue complex, Central to Patagonian Andes transition (38°S), *J. South Am. Earth Sci.*, *22*(1-2), 66–88, doi:10.1016/j.jsames.2006.08.008.

Melnick, D., B. Bookhagen, M. R. Strecker, and H. P. Echtler (2009), Segmentation of megathrust rupture zones from fore-arc deformation patterns over hundreds to millions of years , Arauco peninsula , Chile, , *114*, 1–23, doi:10.1029/2008JB005788.

Moreno, M. et al. (2011), Heterogeneous plate locking in the South-Central Chile subduction zone: Building up the next great earthquake, *Earth Planet. Sci. Lett.*, *305*(3-4), 413–424, doi:10.1016/j.epsl.2011.03.025.

Moreno, M. et al. (2012), Toward understanding tectonic control on the M w 8.8 2010 Maule Chile earthquake, *Earth Planet. Sci. Lett.*, *321-322*, 152–165, doi:10.1016/j.epsl.2012.01.006.

Mpodozis, C., Ramos, V., (1989), The Andes of Chile and Argentina. Geology of the Andes an its relation to Hydrocarbon and Mineral Resources. *Circumpacific Council for Energy and Mineral Resourves*, Earth Sciences Series, 11, p.59-90.

Mpodozis, C., and P. Cornejo (2012), Cenozoic Tectonics and Porphyry Copper Systems of the

Chilean Andes, , 329–360.

Murdie, R. E., D. J. Prior, P. Styles, S. S. Flint, R. G. Pearce, and S. M. Agar (1993), Seismic responses to ridge-transform subduction:Chile triple junction, *Geology*, *21*, 1095, doi:10.1130/0091-7613(1993)021<1095:SRTRTS>2.3.CO;2.

Nakamura, K., K. H. Jacob, and J. N. Davies (1977), Volcanoes as possible indicators of tectonic stress orientation - Aleutians and Alaska, *Pure Appl. Geophys. PAGEOPH*, *115*(1-2), 87–112, doi:10.1007/BF01637099.

Newman, P., W. A. Griffith, (2014), The work budget of rough faults, *Tectonophysics*, (636, 1), p 100-110, doi.org/10.1016/j.tecto.2014.08.00.

Norini, G., Baez W., Becchio R., Viramonte J., Giordano G., Arnosio M., Pinton A., Groppelli G., (2013)., The Calama–Olacapato–El Toro fault system in the Puna Plateau, Central Andes: Geodynamic implications and stratovolcanoes emplacement, Tectonophysics.doi./10.1016/j.tecto.2013.06.013

Okada, B. Y. Y. (1992), Internal deformation due to shear and tensile faults in a half-space, , *82*(2), 1018–1040.

Okada, B. Y. Y. (1985), Surface deformation due to shear and tensile faults in a half-space, , *75*(4), 1135–1154.

Pan, E., Yuan, J. H., Chen, W.Q., Griffith, W.A., (2014), Elastic deformation due to polygonal dislocations in a transversely isotropic half-space, *Bull. Seismol. Soc. Am.*, *104*(6), 2698–2716, doi:10.1785/0120140161.

Pardo-Casas, F., Molnar, P., (1997).Relative motion of the Nazca (Farallón) and South American plates since late Cretaceous times, *Tectonics 6*, 233–248.

Pérez-Flores, P., Cembrano J., Sáncez-Alfaro, P., Veloso, E., Arancibia, G., Roquer, T., (2016), Tectonics, magmatism and paleo-fluid distribution in a strike-slip setting: Insights from the northern termination of the Liquiñe-Ofqui Fault System, Chile.*Tectonophysics*.doi:10.1016/j.tecto.2016.05.016.

Peacock S.M., (1991), Numerical simulations of subduction zone pressure-temperature-time paths: constraints on fluid production and arc magmatism. Philosophical Transactions of the *Royal Society, London* A335, 341-353.

Piquer, J., J. Skarmeta, and D. R. Cooke (2015), Structural evolution of the Rio Blanco-Los Bronces District, Andes of Central Chile: Controls on stratigraphy, magmatism, and mineralization, *Econ. Geol.*, *110*(8), 1995–2023, doi:10.2113/econgeo.110.8.1995.

Potent, S., (2003), Kinematik und Dynamik neogener Deformationsprozesse des südzentralchilenischen Subduktionssystems, nördlichste Patagonische Anden (37°-40°S), (PhD thesis), University of Hamburg.

Radic, J. P. (2010), Las cuencas cenozoicas y su control en el volcanismo de los Complejos Nevados de Chillán y Copahue-Callaqui (Andes del Sur, 36-39°S), *Andean Geol.*, *37*(1), 220–246, doi:10.4067/S0718-71062010000100009.

Ramos V.A., Barbieri, M., (1989). El volcanismo cenozoico de Huantraico: Edad y relaciones isotópicas iniciales, provincia de Neuquén. *Revista de la Asociación Geológica Argentina, 43*

(2), 210-223.

Ramos VA., Cristallini E., Perez DJ., (2002), The Pampean flat-slab of the Central Andes. *Jour South. Am. Earth. Scien.*15: 59-78.

Ramos, VA.; Folguera, A. (2005). Tectonic evolution of the Andes of Neuquén: Constraints derived from the magmatic are and foreland deformation. In A case study in sequence stratigraphy and basin dynamics. *Geological Society of London*, Special Publication 252: 15-35.

Ramos, V., (2009), Anatomy and global context of the Andes: Main geologic features and the Andean orogenic cycle, *Geolog. Soc Am. Memoir.* 204, 31-65, doi:10.1130/2009.1204(02).

Rojas, C., M. Beck, and R. Burmester (1994), Paleomagnetism of the mid-Tertiary Ayacara Formation, southern Chile: Counterclockwise rotation in a dextral shear zone, *J. South Am. Earth Sci.*, 7(1), 45–56.

Roquer T., (2016), Fault-controlled development of shallow hydrothermal systems, Southern Andes, *Msc Thesis*, Pontificia Universidad Católica de Chile, Santiago.

Rosenau, M., D. Melnick, and H. Echtler (2006), Kinematic constraints on intra-arc shear and strain partitioning in the southern Andes between 38°S and 42°S latitude, *Tectonics*, *25*(4), n/a–n/a, doi:10.1029/2005TC001943.

Ruegg, J. C., A. Rudloff, C. Vigny, R. Madariaga, J. B. de Chabalier, J. Campos, E. Kausel, S. Barrientos, and D. Dimitrov (2009), Interseismic strain accumulation measured by GPS in the seismic gap between Constitución and Concepción in Chile, *Phys. Earth Planet. Inter.*, *175*(1-2), 78–85, doi:10.1016/j.pepi.2008.02.015.

Sánchez, P., P. Pérez-Flores, G. Arancibia, J. Cembrano, and M. Reich (2013), Crustal deformation effects on the chemical evolution of geothermal systems: the intra-arc Liquiñe–Ofqui fault system, Southern Andes, *Int. Geol. Rev.*, *55*(11), 1384–1400, doi:10.1080/00206814.2013.775731.

Savage, J. C., (1983), A dislocation model of strain accumulation and release at a subduction zone, *J. Geophys. Res.*, *88*(3), 4984–4996.

Scholz, C.H., (2002), The mechanics of earthquakes and faulting, Cambridge, UK: Cambridge University press.

Sepúlveda, F., A. Lahsen, S. Bonvalot, J. Cembrano, A. Alvarado, and P. Letelier (2005), Morpho-structural evolution of the Cordón Caulle geothermal region, Southern Volcanic Zone, Chile: Insights from gravity and 40Ar/39Ar dating, *J. Volcanol. Geotherm. Res.*, *148*(1-2), 165–189, doi:10.1016/j.jvolgeores.2005.03.020.

Shaw, H.R., (1980), Fracture mechanism of magma transport from the mantle to the surface. Physics of Magmatic Processes. Princeton Uni. Press, pp. 201-264,

Sibson, R.H., (1985), A note on fault reactivation. *J Struct. Geolog.* 7, 751-754.

Sielfeld, G., J. Cembrano, and L. Lara (2016), Transtension driving volcano-edifice anatomy: Insights from Andean transverse-to-the-orogen tectonic domains, *Quat. Int.*, 1–17, doi:10.1016/j.quaint.2016.01.002.

Sipkin, S.A., (1994), Rapid determination of global moment-tensor solutions, *Geoophys. Res.*

Let, v. 21, p. 1667-1670.

Somoza, R., (1998), Updated Nazca (Farallon)-South America relative motions during the last 40 My: Implications for mountain building un the central Andean region. *J. South. Ame. Sciences* 11, 211-215.

Steketee, J., (1958a), On Volterra's dislocations in a semi-infinite elastic medium.*Can. J. Phys.* 36, 192-205.

Stern, C.R., (2004), Active Andean volcanism: its geologic and tectonic setting, *Rev. geol. Chile (31)*,p. 161-206, doi/10.4067/S0716-02082004000200001.

Thomas, A. L. (1993), Poly3D: A three-dimensional, polygonal element, displacement discontinuity boundary element computer program with applications to fractures, faults, and cavities in the Earth's Crust: *M.S. Thesis*, Stanford University, Stanford, CA, 68p.

Thomson, S. N. (2002), Late Cenozoic geomorphic and tectonic evolution of the Patagonian Andes Late Cenozoic geomorphic and tectonic evolution of the Patagonian Andes between latitudes 42 Њ S and 46 Њ S : An appraisal based on fission-track results from the transpressional intr, *Geol. Soc. Am. Bull.*, *114*(9), 1159–1173, doi:10.1130/0016-7606.

Tibaldi, A., A. M. F. A. Lagmay, V. V Ponomareva, and S. Geologiche (2005), Effects of basement structural and stratigraphic heritages on volcano behaviour and implications for human activities (the UNESCO / IUGS / IGCP project 455), , *28*(3), 158–170.

Tikoff, B., C. Teyssier, (1994), Strain modeling of displacement-field partitioning in transpressional orogens, *J. Struct. Geol. (16)*, (1575-1588).

Turcotte, D., and Schubert G., (2014), Geodynamics, Cambridge, UK: Cambridge University press.

Vargas, G., S. Rebolledo, S. Sepúlveda, A. Lahsen, R. Thiele, B. Townley, C. Padilla, R. Rauld, M. J. Herrera, and M. Lara (2013), Submarine earthquake rupture , active faulting and volcanism along the major Liquiñe-Ofqui Fault Zone and implications for seismic hazard assessment in the Patagonian Andes, *Andean Geol.*, *40*(1), 141–171, doi:10.5027/andgeoV40n1-a07.

Vigny, C. et al. (2011), The 2010 Mw 8.8 Maule megathrust earthquake of Central Chile, monitored by GPS., *Science*, *332*(6036), 1417–1421, doi:10.1126/science.1204132.

Wall, R., Gana P., Gutierrez A., (1996), Geología de la Hoja de Santiago, área de San Antonio-Melipilla, regiones de Valparaíso, Metropolitana y del Libertador Bernardo O'Higgins, escala 1:100000. *Servicio Nacional de Geología y Minería, Mapas Geológicos, No 2.*

Wang, K., Y. Hu, M. Bevis, E. Kendrick, R. Smalley, R. B. Vargas, and E. Lauría (2007), Crustal motion in the zone of the 1960 Chile earthquake: Detangling earthquake-cycle deformation and forearc-sliver translation, *Geochemistry, Geophys. Geosystems*, *8*(10), n/a–n/a, doi:10.1029/2007GC001721.

Yáñez, G. A., Gana, P., and Fernández, R. (1998). Origen y significado geológico de la Anomalía Melipilla, Chile central . *Revista geológica de Chile*, p 174-198.

Yañez, G., Cembrano, J., (2004), Role of viscous plate coupling in the late Tertiary Andean tectonics, *J. Geophys. Res. ,109*, B02407, doi:10.1029/2003JB002494.

Yoffe, E., (1960), The angular dislocation. *Phil Mag.* 5, 161-175.

Yu, G. (1993), Slip Partitioning along Major Convergent Plate Boundaries,*Pure Appl. Geophys*. , *140*(2), 183–210.

APPENDIX

A. Comparison of GPS data of interseismic surface deformation with model calculated data

Table A-1. GPS-derived secular rates relative to South America plate with corresponding location, uncertainties and source of the data, and model-calculated secular rates. Misfit in magnitude (%) and angular misfit are shown for each site in the data set. Angular misfitis in degrees, clockwisemisfit positive.

Table S1.										
Position		GPS Secular Rates (m/yr)		Uncertainties (m/yr)		Model calculated Secular Rates (m/yr)		Misfit		Source of GPS data
Lat	Long	Ve	Vn	Se	Sn	Ve	Vn	Magnitude (%)	Angular (°)	
-33.447	-70.537	0.1479	0.00717	0.00414	0.00413	0.1555	0.06014	12.60	-18.4	*Lin et al.*, 2013
-30.263	-71.487	0.1844	0.08025	0.00826	0.00768	0.2922	0.09428	52.67	5.6	*Lin et al.*, 2013
-31.602	-68.233	0.06782	0.02877	0.02504	0.02487	0.1403	0.02959	94.63	11.1	*Lin et al.*, 2013
-31.188	-70.999	0.21216	0.06604	0.00982	0.00973	0.2428	0.08252	15.41	-1.5	*Lin et al.*, 2013
-31.398	-71.458	0.25474	0.0755	0.01586	0.0156	0.2731	0.09704	9.08	-3.1	*Lin et al.*, 2013
-35.331	-72.412	0.35383	0.10767	0.00649	0.00637	0.2517	0.09182	27.56	-3.1	*Lin et al.*, 2013
-36.844	-73.025	0.32839	0.1081	0.00342	0.00339	0.2538	0.09432	21.68	-2.2	*Lin et al.*, 2013
-27.385	-70.338	0.22147	0.07041	0.00656	0.00649	0.245	0.06323	8.88	3.2	*Lin et al.*, 2013
-29.102	-71.41	0.29805	0.07507	0.04296	0.02814	0.3108	0.09129	5.39	-2.2	*Lin et al.*, 2013
-33.457	-70.664	0.20819	0.062	0.0038	0.00375	0.189	0.07087	7.08	-4.0	*Lin et al.*, 2013
-31.147	-71.663	0.29234	0.08926	0.01385	0.01369	0.2952	0.102	2.18	-2.1	*Lin et al.*, 2013
-29.977	-70.094	0.17249	0.05472	0.01444	0.01439	0.209	0.05929	20.05	1.8	*Lin et al.*, 2013
-29.908	-71.246	0.18584	0.0813	0.00799	0.00784	0.2788	0.08625	43.87	6.4	*Lin et al.*, 2013
-31.909	-71.514	0.22682	0.06868	0.00428	0.00411	0.2683	0.09659	20.32	-3.0	*Lin et al.*, 2013
-35.810	-70.821	0.17783	0.06076	0.00707	0.00657	0.1501	0.05931	14.12	-2.7	*Lin et al.*, 2013
-33.135	-68.788	0.08356	0.0214	0.01232	0.01226	0.1301	0.03819	57.19	-2.0	*Lin et al.*, 2013

-32.844	-68.796	0.07239	0.02215	0.01103	0.01103	0.1339	0.03778	83.78	1.3	*Lin et al.*, 2013
-32.949	-69.021	0.08409	0.02626	0.01208	0.01206	0.1371	0.04126	62.52	0.6	*Lin et al.*, 2013
-32.952	-69.169	0.09023	0.02893	0.01464	0.01441	0.1404	0.04353	55.13	0.6	*Lin et al.*, 2013
-33.255	-68.150	0.06862	-0.01009	0.01375	0.01374	0.1177	0.03021	75.20	-6.0	*Lin et al.*, 2013
-30.604	-71.204	0.20688	0.07814	0.00952	0.00936	0.2642	0.0876	25.86	2.3	*Lin et al.*, 2013
-30.839	-70.689	0.19092	0.0757	0.01026	0.01008	0.228	0.0734	16.62	3.8	*Lin et al.*, 2013
-30.675	-71.635	0.22788	0.08104	0.00889	0.02607	0.2984	0.1009	30.24	0.9	*Lin et al.*, 2013
-32.835	-70.130	0.18305	0.05829	0.00335	0.0033	0.1721	0.06081	4.99	-1.8	*Lin et al.*, 2013
-33.654	-71.613	0.27105	0.09319	0.02841	0.02807	0.2432	0.08993	9.53	-1.3	*Lin et al.*, 2013
-32.977	-71.015	0.23849	0.07672	0.03957	0.03956	0.2173	0.08002	7.57	-2.4	*Lin et al.*, 2013
-33.150	-70.669	0.21172	0.06279	0.00335	0.00329	0.1939	0.07176	6.38	-3.8	*Lin et al.*, 2013
-29.255	-70.739	0.20957	0.05187	0.0374	0.03739	0.255	0.07328	22.89	-2.1	*Lin et al.*, 2013
-31.777	-70.963	0.21825	0.06269	0.00415	0.0041	0.2317	0.08101	8.09	-3.2	*Lin et al.*, 2013
-30.170	-70.806	0.1793	0.07626	0.00868	0.00856	0.2442	0.07484	31.08	6.0	*Lin et al.*, 2013
-28.572	-70.764	0.25461	0.03734	0.02047	0.02042	0.2652	0.07595	7.20	-7.6	*Lin et al.*, 2013
-33.028	-71.635	0.27772	0.11781	0.0054	0.00529	0.2584	0.09537	8.70	2.7	*Lin et al.*, 2013
-33.354	-70.249	0.18026	0.05223	0.00332	0.00328	0.1702	0.06286	3.32	-4.1	*Lin et al.*, 2013
-40.772	-72.195	0.1445	0.2594	0.0039	0.0085	0.1414	0.0666	47.36	35.7	*Wang et al.*, 2007
-45.914	-71.692	-0.0803	-0.0036	0.0041	0.0062	0.09195	0.01345	15.61	-5.8	*Wang et al.*, 2007
-40.587	-73.733	0.1722	0.1013	0.0034	0.0039	0.2336	0.09859	26.91	7.6	*Wang et al.*, 2007
-42.014	-71.204	-0.0793	0.0063	0.0051	0.0109	0.102	0.03506	35.58	-14.4	*Wang et al.*, 2007
-36.138	-72.802	0.3901	0.1176	0.0052	0.0085	0.2558	0.09251	33.24	-3.1	*Wang et al.*, 2007
-46.538	-71.733	-0.0459	0.0143	0.0033	0.0037	0.08262	0.005961	72.30	13.2	*Wang et al.*, 2007
-42.855	-72.799	-0.0864	0.0345	0.0018	0.0019	0.152	0.06763	78.82	-2.2	*Wang et al.*, 2007
-45.514	-71.892	-0.0498	-0.002	0.0009	0.0013	0.1009	0.02093	106.76	-9.4	*Wang et al.*, 2007
-41.41	-73.799	0.1145	0.0904	0.0023	0.004	0.2292	0.09835	70.96	15.1	*Wang et al.*, 2007
-37.709	-71.822	0.1238	0.0125	0.0039	0.0038	0.1638	0.06511	41.66	-15.9	*Wang et al.*, 2007
-37.579	-73.643	0.336	0.1238	0.0027	0.0032	0.2881	0.107	14.17	-0.1	*Wang et al.*, 2007
-43.896	-73.749	0.0029	0.0622	0.0022	0.0018	0.1952	0.08257	240.38	64.4	*Wang et al.*, 2007

-39.87	-73.402	0.138	0.0389	0.0043	0.0066	0.2213	0.09175	67.09	-6.8	*Wang et al.*, 2007
-45.457	-69.67	-0.0407	0	0.0045	0.006	0.05945	0.003531	46.33	-3.4	*Wang et al.*, 2007
-43.62	-71.808	0.0654	0.0114	0.008	0.0064	0.1099	0.03617	74.28	-8.3	*Wang et al.*, 2007
-41.998	-72.435	-0.1025	0.0633	0.0035	0.008	0.1418	0.06567	29.72	6.8	*Wang et al.*, 2007
-43.753	-69.642	-0.0488	0.0028	0.0093	0.0091	0.07397	0.01199	53.30	-5.9	*Wang et al.*, 2007
-35.786	-71.347	0.2765	0.0504	0.0041	0.0025	0.1716	0.06794	34.33	-11.3	*Wang et al.*, 2007
-36.917	-71.431	0.1359	-0.0509	0.0068	0.0159	0.1591	0.05794	16.68	0.5	*Wang et al.*, 2007
-36.736	-72.771	0.2912	0.0928	0.0133	0.0105	0.2011	0.07673	29.57	-3.2	*Moreno et al.*, 2011
-38.769	-72.639	0.1189	0.1041	0.0098	0.0073	0.2539	0.09243	70.98	21.2	*Moreno et al.*, 2011
-36.772	-73.211	0.344	0.0982	0.021	0.0308	0.1597	0.062	52.11	-5.3	*Moreno et al.*, 2011
-39.754	-73.388	0.1678	0.1139	0.032	0.005	0.2525	0.09191	32.50	14.2	*Moreno et al.*, 2011
-41.806	-74.027	0.2039	0.0763	0.0135	0.0054	0.2507	0.09225	22.70	0.3	*Moreno et al.*, 2011
-37.723	-73.664	0.2947	0.1282	0.028	0.0282	0.1744	0.06888	41.65	2.0	*Moreno et al.*, 2011
-37.93	-73.321	0.2123	0.0789	0.0238	0.02	0.2194	0.08345	3.64	-0.4	*Moreno et al.*, 2011
-40.949	-73.721	0.1952	0.0942	0.0094	0.0056	0.1324	0.05085	34.56	4.8	*Moreno et al.*, 2011
-45.09	-74.286	0.1408	0.0393	0.0152	0.0315	0.2198	0.08648	61.58	-5.9	*Moreno et al.*, 2011
-37.896	-71.346	0.1028	-0.0512	0.0114	0.0087	0.1471	0.05647	37.20	5.5	*Moreno et al.*, 2011
-37.607	-72.689	0.2067	0.0562	0.0275	0.014	0.2936	0.1056	45.66	-4.6	*Moreno et al.*, 2011
-37.824	-73.031	0.1551	0.0829	0.0244	0.0321	0.2581	0.09692	56.77	7.5	*Moreno et al.*, 2011
-40.59	-73.142	0.1102	0.0426	0.0123	0.016	0.1656	0.06458	50.45	-0.2	*Moreno et al.*, 2011
-39.679	-72.307	0.0614	0.0303	0.0177	0.002	0.1745	0.06878	173.94	4.8	*Moreno et al.*, 2011
-40.547	-73.72	0.2182	0.0865	0.0135	0.0077	0.2078	0.0794	5.23	0.7	*Moreno et al.*, 2011
-38.242	-73.491	0.2372	0.0826	0.0174	0.0126	0.1897	0.07508	18.77	-2.4	*Moreno et al.*, 2011
-36.663	-71.321	0.1921	0.0293	0.0078	0.0087	0.2551	0.09455	40.00	-11.7	*Moreno et al.*, 2011
-36.836	-72.361	0.281	0.0489	0.0147	0.0138	0.1939	0.07176	27.51	-10.4	*Moreno et al.*, 2011
-37.206	-72.849	0.2764	0.079	0.0021	0	0.1929	0.0842	26.78	-7.6	*Moreno et al.*, 2011
-38.341	-73.502	0.2096	0.0996	0.025	0.0074	0.1569	0.07014	25.94	1.3	*Moreno et al.*, 2011
-39.349	-73.182	0.1551	0.0753	0.0069	0.003	0.1926	0.07903	20.75	3.6	*Moreno et al.*, 2011
-38.531	-73.238	0.1794	0.0993	0.0058	0.0015	0.2729	0.09824	41.45	9.2	*Moreno et al.*, 2011

-37.338	-71.532	0.1593	-0.0078	0.0001	0.001	0.2226	0.09205	51.03	-19.7	*Moreno et al.*, 2011
-36.741	-72.295	0.2656	0.0839	0.0286	0.0143	0.1418	0.06567	43.90	-7.3	*Moreno et al.*, 2011
-36.844	-73.026	0.3221	0.0903	0.0101	0.0171	0.1873	0.07706	39.46	-6.7	*Moreno et al.*, 2011
-43.566	-74.827	0.4432	0.1022	0.0044	0.0055	0.1591	0.06984	61.80	-10.7	*Moreno et al.*, 2011
-36.746	-73.19	0.3399	0.1079	0.0137	0.0089	0.2447	0.1036	25.49	-5.3	*Moreno et al.*, 2011
-43.897	-73.749	0.0675	0.0318	0.0186	0.0193	0.1253	0.04362	77.81	6.0	*Moreno et al.*, 2011
-38.4	-73.9	0.331	0.076	0.0134	0.0205	0.2858	0.1074	10.10	-7.7	*Moreno et al.*, 2011
-37.175	-72.931	0.3233	0.0933	0.0217	0.0132	0.1541	0.06924	49.79	-8.1	*Moreno et al.*, 2011
-34.72	-72.34	0.2166	0.0663	0.0004	0.0011	0.2941	0.1057	37.96	-2.7	*Moreno et al.*, 2011
−35.307	−71.962	0.3321	0.0924	0.0128	0.0117	0.227	0.09697	28.39	-7.6	*Ruegg et al.*, 2009
−37.245	−73.272	0.3474	0.1715	0.0283	0.0179	0.1453	0.06371	59.05	2.6	*Ruegg et al.*, 2009
−36.639	−72.205	0.2711	0.0853	0.0158	0.0122	0.2253	0.09741	13.63	-5.9	*Ruegg et al.*, 2009
−36.236	−72.812	0.3353	0.1272	0.0154	0.0121	0.143	0.05556	57.22	-0.5	*Ruegg et al.*, 2009
−37.336	−71.625	0.1721	0.0109	0.013	0.0119	0.2132	0.08471	33.04	-18.0	*Ruegg et al.*, 2009
−35.318	−72.415	0.3701	0.1121	0.0149	0.0119	0.2327	0.09147	35.34	-4.6	*Ruegg et al.*, 2009
−35.412	−72.491	0.3523	0.1264	0.0161	0.0125	0.194	0.08277	43.65	-3.4	*Ruegg et al.*, 2009
−35.586	−72.626	0.3525	0.1365	0.0147	0.0122	0.1617	0.06983	53.40	-2.2	*Ruegg et al.*, 2009
−35.828	−72.606	0.3484	0.1292	0.0124	0.0115	0.1253	0.04149	64.48	2.0	*Ruegg et al.*, 2009
−35.843	−72.639	0.36	0.1281	0.016	0.0124	0.12	0.04311	66.63	-0.2	*Ruegg et al.*, 2009
−35.949	−72.744	0.3595	0.133	0.0175	0.0127	0.2443	0.09826	31.30	-1.6	*Ruegg et al.*, 2009
−35.677	−71.347	0.2788	0.0539	0.0123	0.0116	0.1848	0.0754	29.71	-11.3	*Ruegg et al.*, 2009
−35.464	−72.255	0.3536	0.102	0.0162	0.0122	0.2332	0.09828	31.24	-6.8	*Ruegg et al.*, 2009
−35.558	−72.086	0.3365	0.0989	0.0142	0.0121	0.1504	0.06719	53.03	-7.7	*Ruegg et al.*, 2009
−35.616	−71.777	0.3071	0.0706	0.014	0.0125	0.261	0.1028	10.98	-8.6	*Ruegg et al.*, 2009
−35.709	−71.069	0.2319	0.0709	0.0127	0.0117	0.1414	0.06615	35.62	-8.1	*Ruegg et al.*, 2009
−35.815	−70.834	0.1857	0.0299	0.0141	0.0118	0.1546	0.05921	11.98	-11.8	*Ruegg et al.*, 2009
−37.346	−72.333	0.2328	0.0621	0.026	0.0197	0.2067	0.07979	8.04	-6.2	*Ruegg et al.*, 2009
−37.255	−72.697	0.2619	0.1024	0.0162	0.0145	0.2971	0.105	12.06	1.9	*Ruegg et al.*, 2009

−37.192	−73.569	0.4254	0.1469	0.0228	0.0165	0.2601	0.1028	37.86	-2.5	*Ruegg et al.*, 2009
−37.059	−73.142	0.3126	0.136	0.016	0.0124	0.1398	0.06562	54.70	-1.6	*Ruegg et al.*, 2009
−37.330	−71.75	0.1697	0.022	0.0141	0.0122	0.2154	0.0889	36.18	-15.0	*Ruegg et al.*, 2009
−37.411	−71.955	0.1901	0.0364	0.013	0.0119	0.2354	0.09526	31.20	-11.2	*Ruegg et al.*, 2009
−36.410	−72.437	0.3523	0.0522	0.0128	0.0117	0.1555	0.06015	53.19	-12.7	*Ruegg et al.*, 2009
−35.172	−72.269	0.3266	0.1253	0.0137	0.0118	0.2045	0.07846	37.38	0.0	*Ruegg et al.*, 2009
−37.285	−72.942	0.3046	0.1074	0.0162	0.0145	0.2539	0.09434	16.14	-1.0	*Ruegg et al.*, 2009
−35.750	−71.957	0.319	0.0952	0.0124	0.0116	0.2858	0.1198	6.91	-6.1	*Ruegg et al.*, 2009
−36.085	−72.125	0.3041	0.0791	0.0123	0.0115	0.2717	0.09789	8.09	-5.2	*Ruegg et al.*, 2009
−37.256	−73.436	0.3669	0.1427	0.0243	0.0165	0.1952	0.08256	46.16	-1.7	*Ruegg et al.*, 2009
−37.393	−72.231	0.2427	0.0645	0.0214	0.016	0.2906	0.1136	24.25	-6.5	*Ruegg et al.*, 2009
−37.216	−72.384	0.2803	0.0794	0.0163	0.0147	0.1419	0.06569	46.33	-9.0	*Ruegg et al.*, 2009
−36.829	−73.035	0.3412	0.1277	0.0216	0.0167	0.1555	0.06963	53.23	-3.6	*Ruegg et al.*, 2009
−33.457	−70.664	0.2394	0.0786	0.0227	0.0158	0.1736	0.0761	24.77	-5.5	*Ruegg et al.*, 2009
−33.150	−70.669	0.2044	0.0614	0.0079	0.0076	0.2375	0.09237	19.40	-4.5	*Ruegg et al.*, 2009
−16.466	−71.493	0.1712	0.0446	0.045	0.028	0.1947	0.07749	18.45	-7.1	*Ruegg et al.*, 2009